International Journal of Modelling and Simulation

https://www.tandfonline.com/action/journalInformation?journalCode=tjms20

(Editor-in-Chief: Professor Jie Shen - University of Michigan - Dearborn, USA)

Accepted November 27th 2021

COMPUTATION OF REACTIVE MIXED CONVECTION RADIATIVE VISCOELASTIC NANOFLUID THERMO-SOLUTAL TRANSPORT FROM A STRETCHING SHEET WITH JOULE HEATING

MD. Shamshuddin[1*]

[1]*Department of Mathematics, Vaagdevi College of Engineering (Autonomous), Bollikunta, Warangal-506005, Telangana State,* ***India.***
Email: shammaths@gmail.com/shamshuddin_md@vaagdevi.edu.in

S.O. Salawu[2]

[2]*Department of Physical Science, College of Pure and Applied Sciences, Landmark University, Omu-aran,* ***Nigeria****.*
Email: kunlesalawu2@gmail.com

O. Anwar Bég[3]

[3]*Multi-Physical Engineering, Dept. Mechanical/Aeronautical Engineering, Salford University, Manchester, M54WT,* ***UK****.*
Email: gortoab@gmail.com

Ali Kadir[3]

[3]*Multi-Physical Engineering, Dept. Mechanical/Aeronautical Engineering, Salford University, Manchester, M54WT,* ***UK****.*
Email: A. Kadir@salford.ac.uk

Tasveer A. Bég[4]

[4] *Engineering Mechanics Research, Israfil House, Dickenson Rd., Longsight, Manchester, M13,* ***UK****.*
Email: tasveerbeg@gmail.com

***Corresponding author:** shammaths@gmail.com/shamshuddin_md@vaagdevi.edu.in*

ABSTRACT:

As a model for electroconductive nanomaterials processing, the present article examines incompressible mixed convection nanofluid flow with convective heat transport from a stretching sheet under the impact of Joule heating and radiative heat flux. The transformed nonlinear boundary value problem is solved with a robust Chebyshev collocation technique. Validation is conducted with earlier published results. Nanoparticle concentrations are suppressed with increasing chemical reaction parameter and the effect is strongest for copper-water nanofluid and weakest for TiO_2 water nanofluid. Increasing Biot number boosts the temperatures for copper and Al_2O_3 but reduces it for TiO_2 nanoparticles. Increasing heat generation boosts temperatures strongly for Al_2O_3 and TiO_2 nanoparticles but weakly for copper nanoparticles. Greater thermophoresis parameter strongly boosts temperatures but suppresses nanoparticle concentrations.

KEYWORDS: *Maxwell viscoelastic nanofluid; Metallic nanoparticles; non-uniform heat source/sink; Joule heating; thermophoretic diffusion; Brownian motion.*

1. INTRODUCTION

In recent years a growing trend has emerged in field-responsive "smart" polymeric materials which exhibit multiple levels of intelligence and can be tuned to respond to different stimuli in the field. These complex multi-functional materials are known as electro/magneto-active polymers (E/MAPs) [1] and are polymer-based composites which adapt their behaviour to either electrical or magnetic fields with large deformation or tunable mechanical properties. They generally comprise a soft polymer matrix with a filler of magnetic particles. Many interesting studies of such materials have been reported including [2] on co-block polymer arrangement and magnetic anisotropy. Other examples of these types of materials include electromagnetic shape memory polymers (for soft robotic and medical coating applications in which the matrix softens via magnetic inductive heating) [3], integrated multifunctional shape memory electro-polymers [4-7], ferroelectric polymers [8], electromagnetic smart hydrogels [9] and electro-active programmable polymers [10]. The strongly rheological nature of these materials requires advanced constitutive *non-Newtonian* models for their accurate simulations [11]. Viscoelasticity is a key characteristic of such smart materials and many models are available for simulating this type of behaviour which features both viscous and elastic effects. These include the Oldroyd-B model, PPT model, FENE P model etc. [12] which allow a robust framework for capturing different polymeric features such as stress relaxation, retardation, stretching, molecular re-orientation etc. Other models for rheological simulation include the Ostwald-De Waele model (shear thinning/thickening) [13], Eringen micromorphic family of model (which allow particle angular momentum i. e. spin to be captured) [14] and Walters-B short memory fluid model [15]. The multi-physical nature of smart electromagnetic polymers also invokes complex magnetohydrodynamic (MHD) effects. These require models that analyze the interaction of applied magnetic fields (or electrical fields in electrohydrodynamic) with viscous flows. MHD [16] arises in many important coating applications where smart functional materials can offer significant advantages e. g. corrosion control in lead-lithium interfacial flows in nuclear reactors [17], deposition rate regulation in Chromium nitride coatings [18], nonintrusive control of liquid metal flows in commercial steel and aluminium casting and refining operations [19, 20]. *Magneto-viscoelastic coating flow models* have in particular emerged as a key area of recent activity in smart electromagnetic rheological materials analysis. Many interesting theoretical and computational studies of coating flows have been reported in this regard featuring a wide spectrum of non-Newtonian models. Although magnetohydrodynamic body forces is usually of a linear nature, when magnetic induction is neglected, the nonlinear nature of non-Newtonian terms and convective transport necessitates the use of numerical methods to accommodate magnetic functional polymer flows. Khan et al. [21] used the Sisko viscoelastic model and Liao homotopy analysis method (HAM) to study magnetic rheological polymer flow from a radially stretching sheet over a solid undeformable substrate. Gaffar et al. [22] used Keller's finite difference box method to simulate the steady state two-dimensional boundary layer Falkner-Skan coating flow of Eyring-Powell two-parameter rheological functional polymer from a non-isothermal two-dimensional geometry with convective wall heating. Other non-Newtonian hydromagnetic coating smart material flow simulations (either external or internal) have featured the tangent hyperbolic model [23], single and two-phase (dusty) Jeffrey's viscoelastic models [24-26], third order Reiner Rivlin differential model [27], Johnson-Segalman non-affine model [28], Carreau ferromagnetic model [29], viscoelastic micropolar model [30], micromorphic models [31-32]. An alternative model is the upper-convected Maxwell (UCM) viscoelastic fluid which quite accurately describes fluid relaxation time characteristics and also accommodates the shear-dependent viscosity. It is particularly suitable for quantifying fluid elasticity in

incompressible boundary layer polymeric flows. Renardy [33] provided a matched asymptotic analysis of UCM viscoelastic flow in a re-entrant corner, deriving comprehensive similarity solutions and with numerical integration demonstrated that the matched solution satisfies the equations of motion in both the core and wall region. More recently Zhang *et al.* [34] presented homotopy solutions for transient magneto-convective boundary layer flow of Maxwell fluids with wall slip, suction and heat generation/absorption effects. Bhatti et al. [35] used a successive Taylor series linearization technique and MATLAB quadrature to compute the effects of radiative flux and non-Fourier thermal relaxation on hydromagnetic Maxwell polymer coating flow on a stretching horizontal substrate. Further studies of magnetized Maxwell polymer flows include Hayat et al. [36] (on Homann plane stagnation flow), Motsa et al. [37] (on wall suction effects in Sakiadis flow) and Mukhopadhyay [38] (on time-dependent Maxwell stretching wall flow in Darcian porous media with radiative flux).

A significant development in 21st century engineering has been the emergence of nanomaterials. Engineers are increasingly designing systems at the *nanoscale* and important progress has been made in nanotube-embedded gels, nano-lubricants, electro-conductive nano-polymers etc. An important sub-group of liquid nanomaterials is *nanofluids*. Introduced in the 1990s by Choi 1995 [39], these complex fluids were developed primarily to achieve substantial improvements in thermal enhancement. They are synthesized by doping conventional working fluids e. g. water, polymers, ethylene glycol etc., with either metallic or carbon-based nanoparticles with average particle sizes below 100 nm. The resulting colloidal suspension achieves superior thermal conductivity, heat capacity and viscosity properties compared with macroscopic fluids. Applications of nanofluids include marine lubricants, smart functional polymer coatings, jet engine and automotive cooling systems, biomedical pharmacodynamics (where targeted drug delivery can be achieved via precision engineered nanoparticles introduced into the blood stream), direct absorber solar collectors and geotechnical remediation. Computational nanofluid mechanics has also received significant attention in the past decade. A particularly popular formulation has been the Buongiorno [40] two-component nanofluid model which emphasizes Brownian dynamics and thermophoretic body force, the latter driving nanoparticles under a thermal gradient. However, while this model allows for the inclusion of a species diffusion equation for nanoparticles, it does not permit the analysis of actual nanomaterials e. g. copper, zinc, diamond etc. The Tiwari-Das nanoscale model is appropriate for this. When both models are combined (as in the current study), both nanoparticle material and concentration distributions can be studied. The presence of nanoparticles in base fluids has been widely demonstrated to achieve thermal conductivity enhancement. However, it also influences the rheology of nanofluid suspensions. Experimental confirmation of viscoelastic non-Newtonian behavior has been documented by Gonçalves et al. [41]. Hojjat et al. [42] identified pseudoplastic (shear thinning) behavior in γ-Al_2O_3, TiO_2 and CuO nanoparticles dispersed in a 0.5 wt.%. aqueous solution of carboxymethyl cellulose (CMC) base fluid. Further investigations have shown strong rheological properties in for example, graphite/oil nanofluids [43] and copper oxide/lubricant nanofluids [44] (with shear-thinning and aggregation observed under a wide range of conditions). In parallel with these laboratory studies, a number of mathematical and numerical simulations of non-Newtonian nanofluid polymer coating flows have been reported. Many numerical schemes have been implemented in these studies to solve the complex differential equation systems featured in nanoscale magnetic polymer coating transport phenomena. For example, Kumar et al. [45] used the Stokes polar couple stress model and Tiwari–Das nanoscale model with MATLAB quadrature to compute the transient dissipative magnetic copper–water and aluminium oxide–water nanopolymer boundary layer flow from a stretching sheet. Elgazery [46] derived Chebyshev pseudospectral (CPS) method numerical solutions for

Casson viscoplastic non-Newtonian magnetohydrodynamic nanofluid flow with gold and alumina nanoparticles through a non-Darcian porous medium. Mehmood et al. [47] deployed the Reynolds exponential viscosity model and Buongiorno nanoscale model to study the non-orthogonal stagnation flow of a nanopolymer coating with thermal jump and radiative flux conditions. Other rheological nanofluid simulation studies include Rana et al. [48] (variational finite element analysis of second order Reiner-Rivlin dissipative nano-polymer extrusion), Rao et al. [49] (magnetized Casson viscoplastic nanofluid coating heat transfer), Ali et al. [50] (Cross rheological nano-doped thermosolutal blood flow), Nagendra et al. [51] (magnetized Williamson viscoelastic axisymmetric coating flow of a conical body), Khan et al. [52] (Oldroyd-B viscoelastic nanofluid stretching flow and heat transfer). Maxwell viscoelastic nanofluid magnetohydrodynamic flow was considered by Ramesh et al. [53] using the Tiwari-Das volume fraction model. Mustafa et al. [54] have investigated Maxwell viscoelastic flow from an exponentially stretching sheet with nonlinear convection. Hayat et al. [55] have investigated Burgers' fluid in stagnation point flow with Newtonian heating.

In the above studies Joule heating i. e. Ohmic dissipation effects were neglected. These can exert a significant influence on velocity and temperature fields in magnetic nano-polymer flows. In particular they can modify the dissipation of mechanical energy via heating in real flows. Several studies have described Joule dissipation in addition to conventional viscous heating (common in polymeric thermal processing). Shamshuddin et al. [56] used a variational parameter method to compute the collective Ohmic and viscous heating effects in thermo-solutal squeezing magnetized flow in a Riga electromagnetic plate sensor system for a Newtonian fluid, also considering thermal relaxation. Hayat and Qasim [57] studied the collective influence of thermal radiation and thermophoretic body force on Maxwell viscoelastic hydromagnetic flow using a homotopy analysis method. Prasad et al. [58] deployed the Keller box finite difference method to investigate Ohmic and viscous heating effects on hydromagnetic coating flow on a cylinder in Darcy-Forchheimer permeable media. They observed a strong elevation in temperatures at all locations along the cylinder and also a significant thickening of thermal boundary layers. Hayat et al. [59] generated series solution for MHD flow of Burgers' fluid with joule heating. Further Hayat and his co-workers [60] collective radiative and Ohmic heating effects in Eyring-Powell fluid employing series solution.

In the present study, as a simulation of smart electromagnetic functional nano-polymer manufacturing flow, a new mathematical model for incompressible mixed convection flow with convective heat transport from a stretching sheet under the impact of Joule heating and radiative heat flux is described. The current flow model is formulated to consider several different water-based nanofluids with reactive metallic/oxide nanoparticles (Copper, Alumina and Titanium oxide). Uneven heat source/sink, viscous dissipation, thermophoresis, Brownian motion and first order (homogenous and destructive) chemical reaction effects are incorporated in the model. Effectively therefore the Tiwari-Das nanoparticle volume fraction and Buongiorno nanoscale models are combined to furnish a better framework for modelling multiple nanoscale effects. The upper convected Maxwell model is deployed to analyze rheological (viscoelastic) nanofluid behaviour. This non-Newtonian model is valid at both low and high Weissenberg numbers and in particular permits a robust treatment of the viscoelastic boundary layer formed in a thin region closer to the wall in which the relaxation terms are recovered. Furthermore, at high Weissenberg flows it is noteworthy that there is a longer relaxation time which enables the velocity of fluid (nano-polymer) to vanish at the wall and particles away from the wall can move long distances within one relaxation time so that particles

closer to the wall travel only a short distance. Rosseland's diffusion flux model is deployed for radiative transfer. The governing non-linear partial differential equations are rendered into a dimensionless system of coupled ordinary differential equations, with appropriate similarity transformations. The well-posed nonlinear boundary value problem is solved with a robust Chebyshev collocation technique [61-62]. Graphical results for velocity, temperature and nanoparticle concentration distributions are presented for the different metallic-aqueous nanofluid cases. Validation is conducted with earlier published results, showing an excellent correlation. Detailed physical interpretation is included. The current model is therefore novel and features multiple effects in rheological nanofluid coating dynamics which have not been considered simultaneously in the existing literature.

2. MAGNETIC NANOPOLYMER COATING MODEL

Inspired by simulating the functional magnetic nano-polymer coating boundary layer flow on a plane stretching substrate (sheet), we consider 2-D, incompressible and steady laminar mixed convection thermo-solutal flow with Joule heating (Ohmic dissipation) in a reactive Maxwell viscoelastic nanofluid containing different nanoparticles. The magnetic field is static and imposed transversely to the plane of the sheet (substrate). Electrical polarization voltage is neglected on the sheet. The nanoparticles are magnetic and undergo a homogenous, destructive first order chemical reaction. An (x, y) Cartesian coordinate system is adopted (**Figure 1**). The $x-$ axis is directed along the stretching sheet and the $y-$ axis is perpendicular to it. With a stretching velocity which is assumed to be $u = u_w(x) = ax$. Here $a > 0$. The convective surface and ambient temperature of the fluid are T_f and T_∞ respectively. The sheet surface and ambient nanoparticle concentration is C_w and C_∞, and the laminar boundary layer flow occupies the domain $y > 0$. Motion is mobilized in the sheet in the $x-$ direction while holding the origin fixed (extrusion slit point). The properties of the nanofluid (viscoelastic smart polymer) are assumed to be constant.

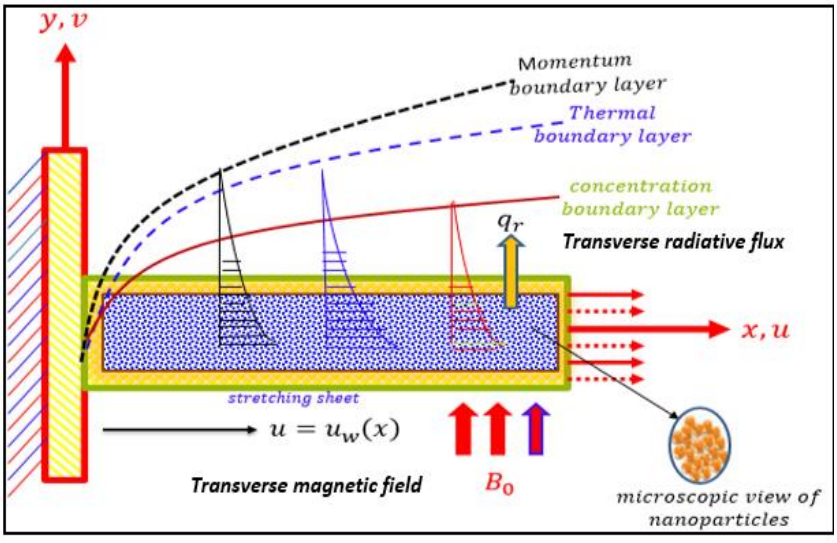

Figure 1: Maxwell magnetic viscoelastic nanofluid polymer stretching flow geometry

The corresponding governing conservation equations, under the above assumptions describing the two-dimensional Maxwell nanofluid boundary layer flow are obtained by amalgamating the previous models of Afify and Elgazery [63] and Sulochana et al. [64] as follows:

$$\frac{\partial u}{\partial u}+\frac{\partial v}{\partial y}=0, \tag{1}$$

$$u\frac{\partial u}{\partial x}+v\frac{\partial u}{\partial y}=\frac{\mu_{nf}}{\rho_{nf}}\frac{\partial^2 u}{\partial y^2}-\Gamma\left(u^2\frac{\partial^2 u}{\partial x^2}+2uv\frac{\partial^2 u}{\partial x\,\partial y}+v^2\frac{\partial^2 u}{\partial y^2}\right)+g\beta\left(T-T_\infty\right)+g\beta^*\left(C-C_\infty\right)-\frac{\sigma_{nf}B_0^2}{\rho_{nf}}\left(u+\Gamma v\frac{\partial u}{\partial y}\right), \tag{2}$$

$$u\frac{\partial T}{\partial x}+v\frac{\partial T}{\partial y}=\frac{k_{nf}}{(\rho c_p)_{nf}}\frac{\partial^2 T}{\partial y^2}-\frac{1}{(\rho c_p)_{nf}}\frac{\partial q_r}{\partial y}+\frac{\mu_{nf}}{(\rho c_p)_{nf}}\left(\frac{\partial u}{\partial y}\right)^2+\frac{\sigma_{nf}B_0^2}{(\rho c_p)_{nf}}u^2+\frac{q'''}{(\rho c_p)_{nf}}+\tau\left\{D_B\frac{\partial T}{\partial y}\frac{\partial C}{\partial y}+\frac{D_T}{T_\infty}\left(\frac{\partial T}{\partial y}\right)^2\right\}, \tag{3}$$

$$u\frac{\partial C}{\partial x}+v\frac{\partial C}{\partial y}=D_B\frac{\partial^2 C}{\partial y^2}+\frac{D_T}{T_\infty}\frac{\partial^2 T}{\partial y^2}-K_r'\left(C-C_\infty\right) \tag{4}$$

The boundary conditions at the substrate (sheet) wall and in the free stream are:

$$at\quad y=0:\ u=U_0=ax,\quad v=0,\quad -k_{nf}\frac{\partial T}{\partial y}=h_f\left(T_f-T\right),\quad C=C_w$$
$$at\ y\to\infty:\ u\to 0,\quad T\to T_\infty,\quad C\to C_\infty \tag{5}$$

In Eqn. (2), Γ is the Maxwell viscoelastic parameter and the Newtonian case is retrieved when $\Gamma\to 0$. The uneven heat source/sink and radiative net heat flux are modelled with the following equations:

$$q'''=\frac{k_f U_0(x)}{x\ \nu_f}\left\{A^*\left(T_f-T_\infty\right)f'+B^*\left(T-T_\infty\right)\right\},\quad \frac{\partial q_r}{\partial y}=-\frac{16\sigma_1}{3k_1}\frac{\partial T^4}{\partial y^2}=-\frac{16\sigma_1 T_\infty^3}{3k_1}\frac{\partial^2 T}{\partial y^2} \tag{6}$$

Employing (6) in equation (3) yields the following form of the energy conservation Eqn. (3):

$$u\frac{\partial T}{\partial x}+v\frac{\partial T}{\partial y}=\frac{k_{nf}}{(\rho c_p)_{nf}}\frac{\partial^2 T}{\partial y^2}+\frac{1}{(\rho c_p)_{nf}}\frac{16\sigma_1 T_\infty^3}{3k_1}\frac{\partial^2 T}{\partial y^2}+\frac{\mu_{nf}}{(\rho c_p)_{nf}}\left(\frac{\partial u}{\partial y}\right)^2+\frac{\sigma_{nf}B_0^2}{(\rho c_p)_{nf}}u^2+\frac{k_f U_0(x)}{(\rho c_p)_{nf}\,x\,\nu_f}\left\{A^*\left(T_f-T_\infty\right)f'+B^*\left(T-T_\infty\right)\right\}+\frac{\left(\rho c_p\right)_s}{\left(\rho c_p\right)_{nf}}\left\{D_B\frac{\partial T}{\partial y}\frac{\partial C}{\partial y}+\frac{D_T}{T_\infty}\left(\frac{\partial T}{\partial y}\right)^2\right\}, \tag{7}$$

Also,

$$\alpha_{nf}=\frac{k_{nf}}{(\rho c_p)_{nf}},\ \rho_{nf}=(1-\phi)\rho_f+\phi\rho_s,\ \mu_{nf}=\frac{\mu_f}{(1-\phi)^{2.5}},\ \nu_f=\frac{\mu_f}{\rho_f},$$
$$(\rho c_p)_{nf}=(1-\phi)(\rho c_p)_f+\phi(\rho c_p)_s, \tag{8}$$
$$k_{nf}=k_f\left[\frac{k_s+2k_f-2\phi\left(k_f-k_s\right)}{k_s+2k_f+2\phi\left(k_f-k_s\right)}\right],\ \sigma_{nf}=\sigma_f\left[1+\frac{3\left(r-1\right)\phi}{\left\{\left(r+2\right)-\left(r-1\right)\phi\right\}}\right],\ r=\frac{\sigma_s}{\sigma_f}$$

In addition to the above, again following Aghamajidi et al. [65], Anwar Beg et al. [66], the thermo physical properties of different base fluid and metallic/oxide nanoparticles based on the Tiwari-Das nanoscale formulation are as given in **Table 1** below.

Table 1: Thermophysical properties of nanoparticles and base fluid

Thermo-physical properties	Base fluid	Nanoparticles		
	$H_2 0$	Cu	$Al_2 0_3$	$Ti0_2$
$\rho\ (Kgm^{-3})$	997.1	8933	3970	4250
$c_p\ (JKg^{-1}K^{-1})$	4179	385	765	686.2
$k\ (Wm^{-1}K^{-1})$	0.613	400	40	8.954
$\alpha \times 10^7\ \ (m^2/s)$	1.47	1163.1	131.7	30.7
$\beta \times 10^{-5}\ \ (K^{-1})$	21	1.67	0.85	0.9
$\sigma\ \ (Sm^{-1})$	0.05	5.96x10^7	3.5x10^7	0.26x10^7
ϕ	0.0	0.05	0.15	0.2

Eqns. (1-5) are formidable to solve even with numerical methods. It is pertinent therefore to simplify them with the help of similarity transformations and dimensionless quantities:

$$\left.\begin{aligned} &\psi(x,y) = \left(\sqrt{a\,\nu_f}\right) x\ f(\eta), \theta\left(\eta\right) = \frac{T-T_\infty}{T_f - T_\infty}, \varphi\left(\eta\right) = \frac{C-C_\infty}{C_f - C_\infty}, \\ &u = \frac{\partial \psi}{\partial y} = a\ x\ f'(\eta),\ \ v = -\frac{\partial \psi}{\partial x} = -\left(\sqrt{a\,\nu_f}\right) f(\eta), \eta = y\left(\sqrt{\frac{a}{\nu_f}}\right) \end{aligned}\right\}, \tag{9}$$

Making use of Eqns. (6-8), then the non-dimensional boundary layer Eqns. (1), (2), (7), (4) emerge as follows wherein the mass conservation (continuity) Eqn. (1) is trivially verified:

Momentum boundary layer Eqn.

$$\begin{aligned} &M_1\ f''' - M_2\left(f'^2 - f\ f'' + \alpha^* f^2\ f''' - 2\alpha^*\ f\ f'\ f''\right) + M_2\ \lambda\left\{\theta + N\varphi\right\} \\ &\qquad - M_3\ M\left\{f' - \alpha^* f\ f''\right\} = 0 \end{aligned} \tag{10}$$

Thermal boundary layer Eqn.

$$\begin{aligned} &\left(M_5 + R\right)\theta'' + M_1\ \mathrm{Pr}\ Ec\ f''^2 + M_3\ \mathrm{Pr}\ Ec\ M\ f'^2 + M_4\ f\ \theta' + \left\{A^* f' + B^*\theta\right\} \\ &\qquad + M_4\ \mathrm{Pr}\left\{Nb\ \theta'\varphi' + Nt\ \theta'^2\right\} = 0 \end{aligned} \tag{11}$$

Nano-particle species boundary layer Eqn.

$$\varphi'' + \frac{Nt}{Nb}\theta'' + Le\ \mathrm{Pr}\left\{f\ \varphi' - Kr\ \varphi\right\} = 0 \tag{12}$$

The corresponding boundary conditions (5) assume the following form:

$$\left.\begin{aligned} &f = 0, \quad f' = 1, \quad \theta' = -Bi\left(1-\theta\right), \ \ \varphi = 1 \quad \ at\ \ \eta = 0 \\ &f' \to 0, \quad \theta \to 0, \quad \varphi \to 0 \quad\ \ when\ \eta \to \infty \end{aligned}\right\} \tag{13}$$

Here:

$$M_1 = (1-\phi)^{-2.5},\ M_2 = \left(1-\phi+\phi\frac{\rho_s}{\rho_f}\right),\ M_3 = \left\{1+\frac{3(r-1)\phi}{\{(r+2)-(r-1)\phi\}}\right\},$$
$$M_4 = \left(1-\phi+\phi\frac{(\rho c_p)_s}{(\rho c_p)_f}\right),\ M_5 = \frac{k_{nf}}{k_f},\ \alpha^* = \alpha\,\Gamma,\ r = \frac{\sigma_s}{\sigma_f} \tag{14}$$

The dimensionless parameters arising in Eqns. (10)-(13) i. e. $\lambda, N, M, R, \Pr, Ec, Nb, Nt, Le$ and Kr. All the notations used aforesaid are inserted in *Appendix*.

The dimensionless flow parameters arising in Eqns. (10)-(14) have the following mathematical definitions:

$$\left.\begin{aligned}
&\lambda = \frac{Gr_x}{\mathrm{Re}_x^2},\quad Gr_x = \frac{g\beta(T_f - T_\infty)x^3}{\nu_f^2}, N = \frac{\beta^*(C_f - C_\infty)}{\beta(T_f - T_\infty)},\quad M = \frac{\sigma_f B_0^2}{a\,\rho_f},\\
&R = \frac{16\sigma_1}{3k_1k_f}T_\infty^3,\ \Pr = \frac{k_f}{(\rho c_p)_f \nu_f}, Ec = \frac{U_0^2}{(c_p)_f(T_f - T_\infty)}, Nt = \frac{\tau D_T(T_f - T_\infty)}{T_\infty \nu_f},\\
&Nb = \frac{\tau D_B(C_f - C_\infty)}{\nu_f},\quad Le = \frac{\alpha_f}{D_B},\quad Kr = \frac{K_r^*}{a},\qquad Bi = \frac{h_f}{k_{nf}}\sqrt{\frac{\nu_f}{a}}
\end{aligned}\right\}, \tag{15}$$

The shear stress, rate of heat transfer and rate of nanoparticle mass transfer at the sheet surface (wall) are defined as, respectively:

$$\left.\begin{aligned}
\tau_w = \mu_f\{1+\alpha\}\left(\frac{\partial u}{\partial y}\right)\Big|_{y=0},\ q_w = -\left(k_{nf} + \frac{16\sigma_1 T_\infty^3}{3k_1}\right)\left(\frac{\partial T}{\partial y}\right)\Big|_{y=0},\ J_w = -D_B\left(\frac{\partial C}{\partial y}\right)\Big|_{y=o}
\end{aligned}\right\} \tag{16}$$

The corresponding dimensionless skin friction, Nusselt number and Sherwood number are given by:

$$\left.\begin{aligned}
&C_f = \frac{\tau_w}{\rho_f U_0^2}\Big|_{y=0} \Rightarrow \sqrt{\mathrm{Re}_x}C_f = -(1+\alpha^*)\ f''(0),\\
&Nu_x = -\frac{x\,q_w}{k_f(T_f - T_\infty)} \Rightarrow \frac{Nu_x}{\sqrt{\mathrm{Re}_x}} = -(M_5 + R)\theta'(0),\\
&Sh_x = \frac{x\,J_w}{D_B(C_f - C_\infty)} \Rightarrow \frac{Sh_x}{\sqrt{\mathrm{Re}_x}} = -\varphi'(0)
\end{aligned}\right\} \tag{17}$$

Here $\mathrm{Re}_x = xU_w/\nu_f$ represents the local Reynolds number (based on stream wise coordinate, x, along the sheet).

3. CHEBYSHEV COLLOCATION NUMERICAL SOLUTION

The transformed dimensionless boundary layer equations (10)-(13) have been solved by applying the Chebyshev collocation method as described in [57 and 61]. Once the velocity, temperature and nanoparticle concentration variables i. e. $f(\eta), \theta(\eta)$ and $\varphi(\eta)$ are evaluated, then skin friction, Nusselt number and Sherwood numbers may be readily computed, based on Eqn. (17).

a. Application of the solution technique

A basis solution is assumed for the unknown functions $f(\eta), \theta(\eta)$ and $\varphi(\eta)$ as a sum for the Chebyshev trial function in the form:

$$f(\eta) = \sum_{i=0}^{N} a_i H_i\left(\frac{2\eta}{J} - 1\right),$$
$$\theta(\eta) = \sum_{i=0}^{N} b_i H_i\left(\frac{2\eta}{J} - 1\right), \tag{18}$$
$$\varphi(\eta) = \sum_{i=0}^{N} c_i H_i\left(\frac{2\eta}{J} - 1\right)$$

In Eqn. (18) a_i, b_i and c_i are the unknown constants which are to be obtained. The term $H_i\left(\frac{2\eta}{J} - 1\right)$ is the *Chebyshev shift trial function* ranging from [-1, 1] to [0, J] where *J* denotes the far stream of the boundary layer. The trial functions are imposed on the boundary conditions (13) and the associated definitions are:

$$\left[\sum_{i=0}^{N} a_i H_i\left(\frac{2\eta}{J} - 1\right)\right]_{\eta=0} = 0, \tag{19}$$

$$\left[\frac{d}{d\eta}\sum_{i=0}^{N} a_i H_i\left(\frac{2\eta}{J} - 1\right) - 1\right]_{\eta=0} = 0, \tag{20}$$

$$\left[\frac{d}{d\eta}\sum_{i=0}^{N} b_i H_i\left(\frac{2\eta}{J} - 1\right) + Bi\left(1 - \sum_{i=0}^{N} b_i H_i\left(\frac{2\eta}{J} - 1\right)\right)\right]_{\eta=0} = 0, \tag{21}$$

$$\left[\sum_{i=0}^{N} c_i H_i\left(\frac{2\eta}{J} - 1\right) - 1\right]_{\eta=0} = 0, \tag{22}$$

$$\left[\sum_{i=0}^{N} a_i H_i\left(\frac{2\eta}{J} - 1\right) - 1\right]_{\eta=J} = 0, \tag{23}$$

$$\left[\sum_{i=0}^{N} b_i H_i\left(\frac{2\eta}{J} - 1\right) - 1\right]_{\eta=J} = 0, \tag{24}$$

$$\left[\sum_{i=0}^{N} c_i H_i\left(\frac{2\eta}{J} - 1\right) - 1\right]_{\eta=J} = 0, \tag{25}$$

Also, using the trial functions, the transformed boundary layer Eqns. (10)-(12) feature the residual equations $R_f\left(\eta, a_i, b_i\right)$, $R_\theta\left(\eta, a_i, b_i, c_i\right)$ and $R_\varphi\left(\eta, a_i, b_i, c_i\right)$. The residual equations are minimized to as close to zero as possible, using the collocation technique as given below:

$$\delta\left(\eta - \eta_r\right) = \begin{cases} 1, & \eta = \eta_r \\ 0, & otherwise \end{cases} \tag{26}$$

$$\int_0^J R_f \delta\left(\eta - \eta_r\right) d\eta = R_f\left(\eta_r\right) = 0, \qquad for \quad r = 1, 2, 3, ..., N-1 \tag{27}$$

$$\int_0^J R_\theta \delta\left(\eta - \eta_r\right) d\eta = R_\theta\left(\eta_r\right) = 0, \qquad for \quad r = 1, 2, 3, ..., N-1 \tag{28}$$

$$\int_0^J R_\varphi \delta\left(\eta - \eta_r\right) d\eta = R_\varphi\left(\eta_r\right) = 0, \qquad for \quad r = 1, 2, 3, ..., N-1 \tag{29}$$

Here $\eta_r = \frac{J}{2}\left(1-\cos(r\pi/N)\right)$ represents the Gauss-Lobatto re-mapped point. The obtained boundary polynomials and the collocated residual equations yield a system of algebraic equations of order *3N+3* which are solved to determine the unknown coefficients a_i, b_i and c_i. This algebraic system of equations is solved by Newton's method to produce the unknown constants. To ensure that the computational solutions match asymptotically with the far boundary field, the value of *J* is chosen for the consistence and convergence of the solutions. The numerics are executed in Maple symbolic software which provides the complete solutions to the problem.

b. Validation and computational results

To benchmark the validity of the Chebyshev collocation method solutions, local Nusselt and Sherwood numbers with different thermophoresis parameter values, *Nt* are compared with previously published results (Afify and Elgazery [63] and Sulochana et al. [64]) and documented in **Table 2**. Very close correlation is achieved and therefore there is high confidence in the Chebyshev collocation method.

Table 2: Computed results validation for the quantities Nu_x and Sh_x

Nt	Sulochana et al. [64]		Afify and Elgazery [63]		Present Chebyshev collocation method results	
	Nu_x	Sh_x	Nu_x	Sh_x	Nu_x	Sh_x
0.1	0.0929123	2.2774434	0.09291	2.27744	0.0928722	2.2773736
0.2	0.0727051	2.2490521	0.07271	2.24905	0.0727699	2.2489993
0.3	0.0925112	2.2228202	0.09251	2.22282	0.0924881	2.2224791
0.4	0.0923202	2.199121	0.09232	2.19921	0.0923021	2.1990789
0.5	0.0921010	2.1783112	0.09210	2.17831	0.0920675	2.1783664

4.GRAPHICAL RESULTS AND DISCUSSION

Extensive numerical MAPLE computations have been performed and all results are visualized in **Figs. 2-18** (velocity distribution $f(\eta)$, temperature distribution $\theta(\eta)$ and concentration distribution $\varphi(\eta)$ for water -based Cu, Al_2O_3 and TiO_2 Maxwell nanofluids) and **Tables 3-5** (local skin friction, Nusselt number and Sherwood number). These results are obtained for variation in dimensionless mixed convection parameter (λ), elastic parameter (α^*), magnetic field intensity parameter (M), radiation-conduction parameter (R), Prandtl number (Pr),Eckert number (Ec),space dependent heat source/sink (A^*), time dependent heat source/sink (B^*), Thermophoresis parameter (Nt) , Brownian motion parameter (Nb), Lewis number (Le), chemical reaction parameter (Kr) and Biot number (Bi). The fixed values of the parameter during solution are $\lambda = 0.5, N = 0.3, M = 1, R = 0.5, Ec = 0.01, A^* = 0.1, B^* = 0.1, Nb = 0.5, Nt = 0.5, \varphi = 0.01, \mathrm{Pr} = 1/0.71,$ $Le = 2, Bi = 0.3$ respectively. All data is carefully selected from appropriate sources to reflect realistic rheological magnetic nanopolymer flow behavior- see [67]-[69].

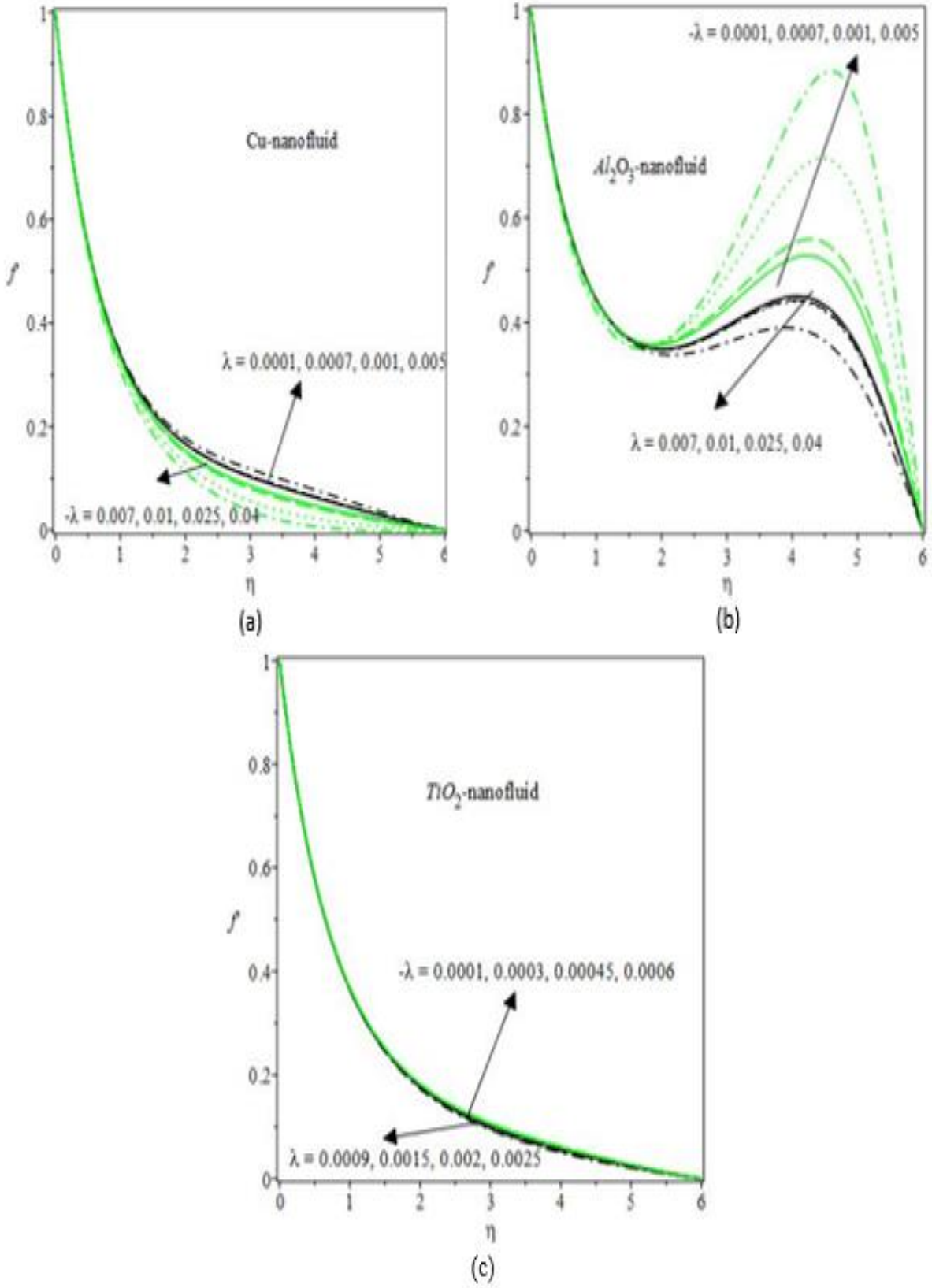

Fig. 2. Profile of $f(\eta)$ for different values of λ ($\lambda < 0$ opposing flow and $\lambda > 0$ assisting flow) (a) for Cu (b) for Al_2O_3 (c) for TiO_2

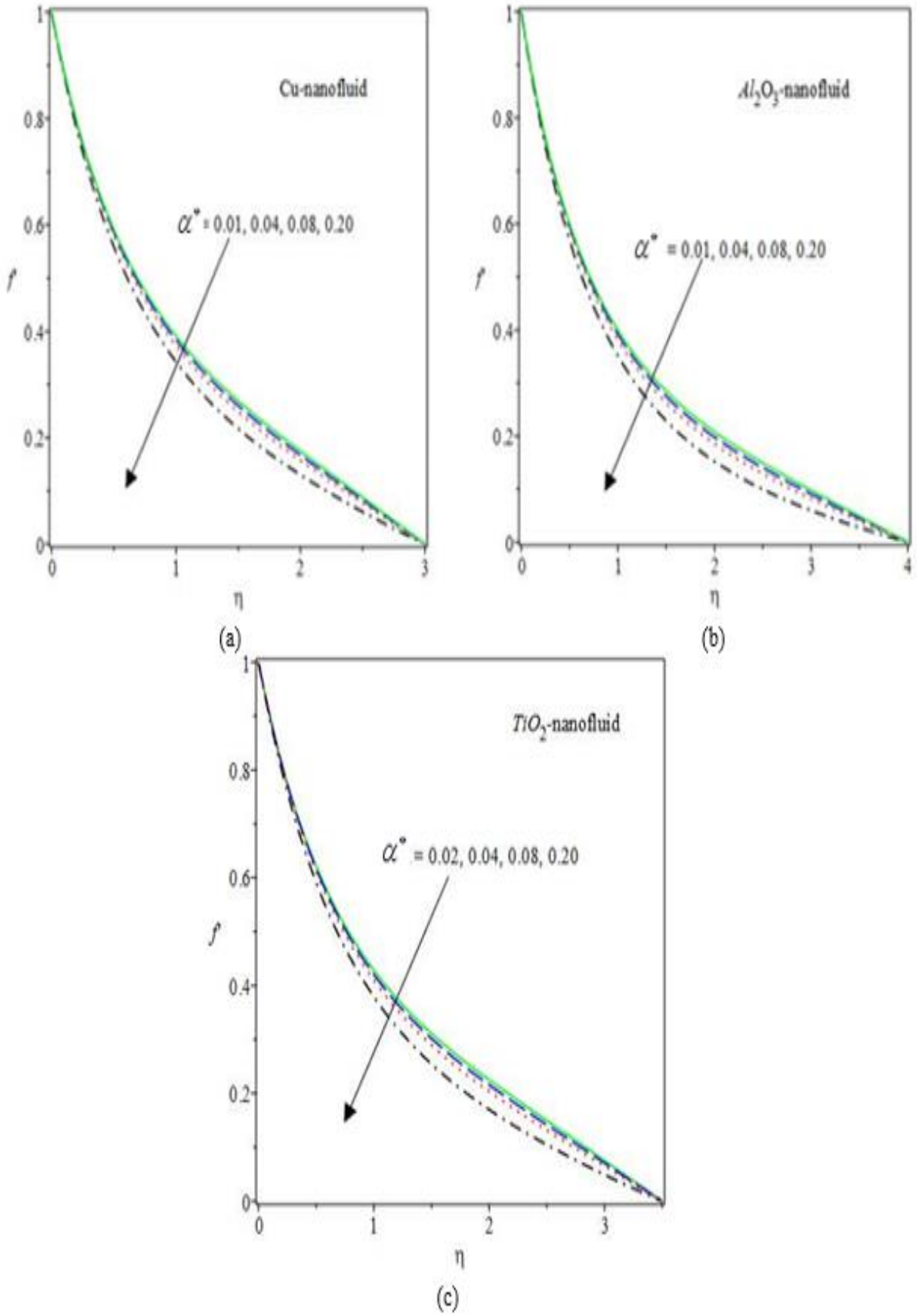

Fig. 3. Profile of $f'(\eta)$ for different values of α^* (a) for Cu (b) for Al_2O_3 (c) for TiO_2

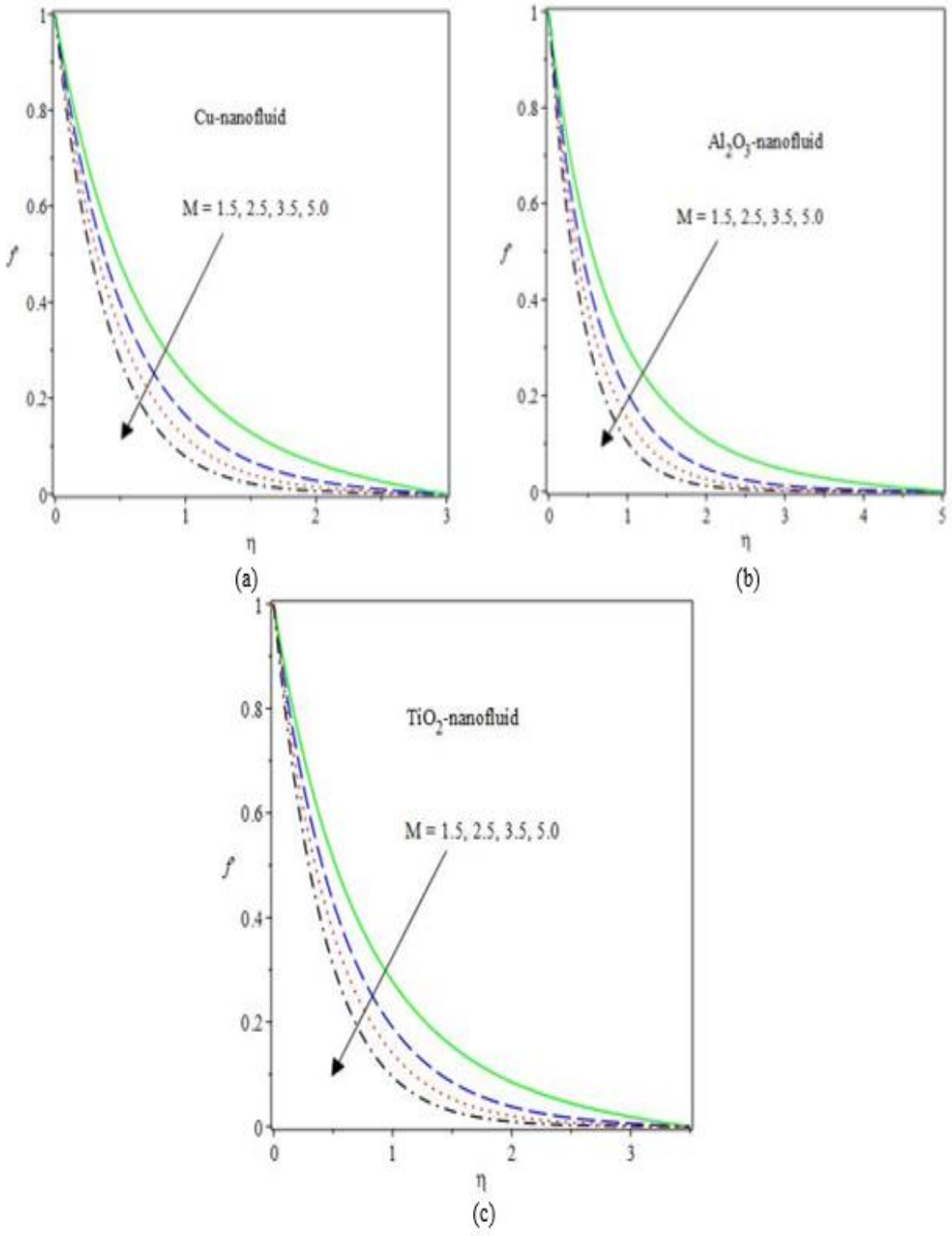

Fig. 4. Profile of $f'(\eta)$ for different values of M (a) for Cu (b) for Al_2O_3 (c) for TiO_2

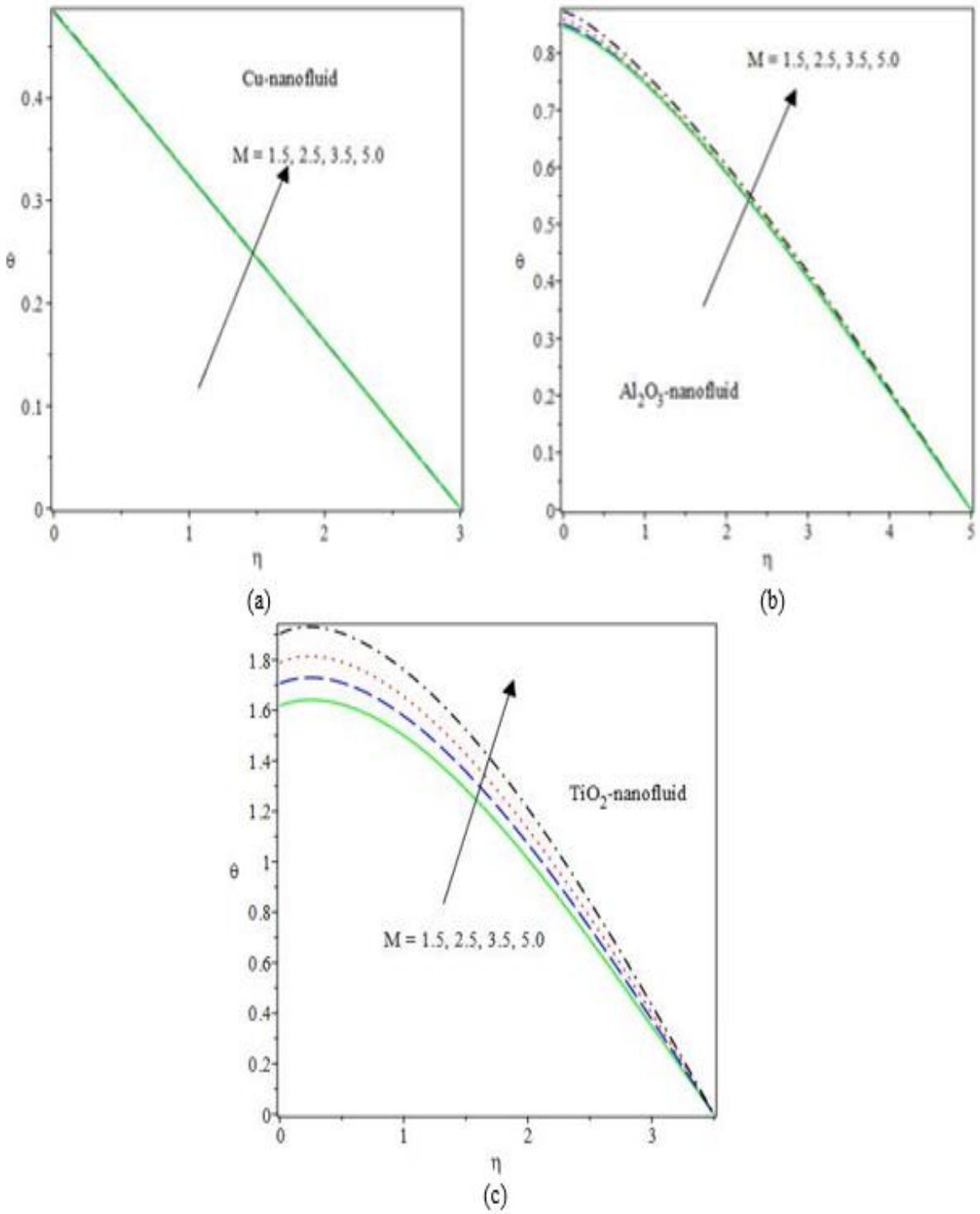

Fig. 5. Profile of $\theta(\eta)$ for different values of M (a) for Cu (b) for Al_2O_3 (c) for TiO_2

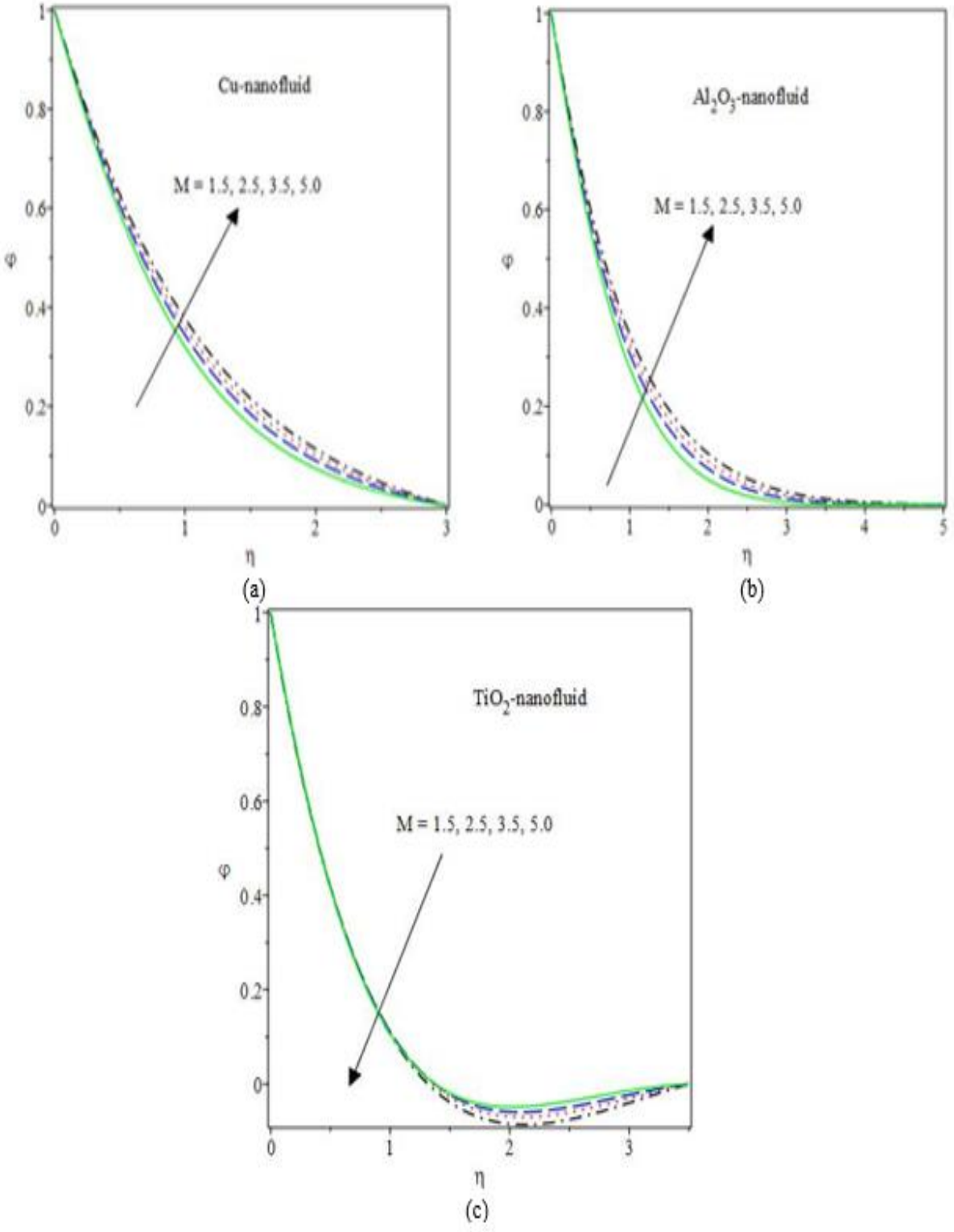

Fig. 6. Profile of $\varphi(\eta)$ for different values of M (a) for Cu (b) for Al_2O_3 (c) for TiO_2

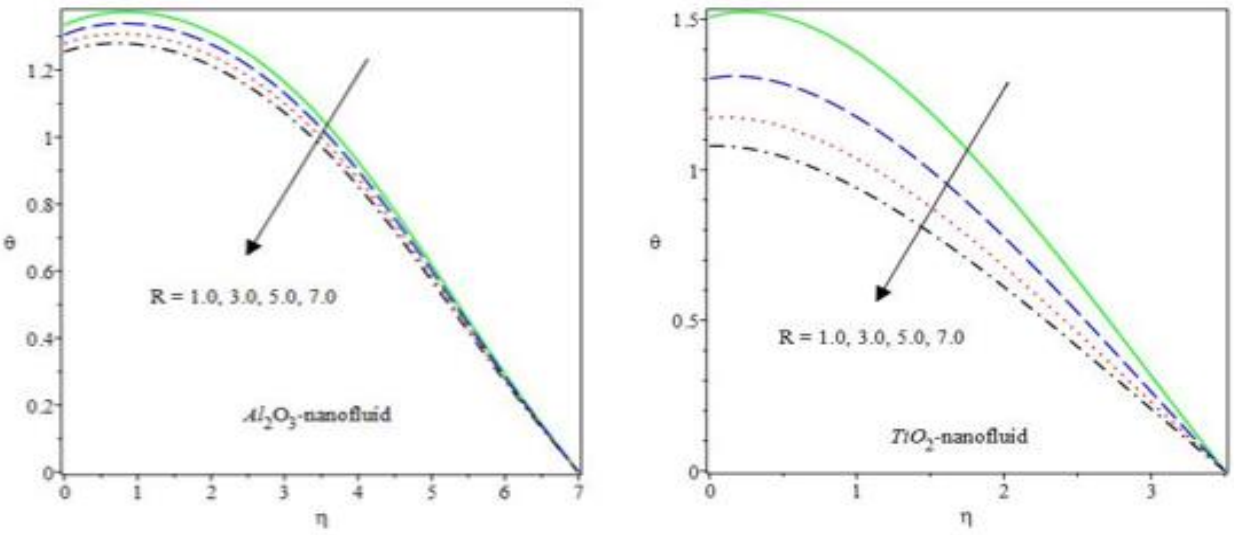

Fig. 7. Profile of $\theta(\eta)$ for different values of R (a) for Al_2O_3 (b) for TiO_2

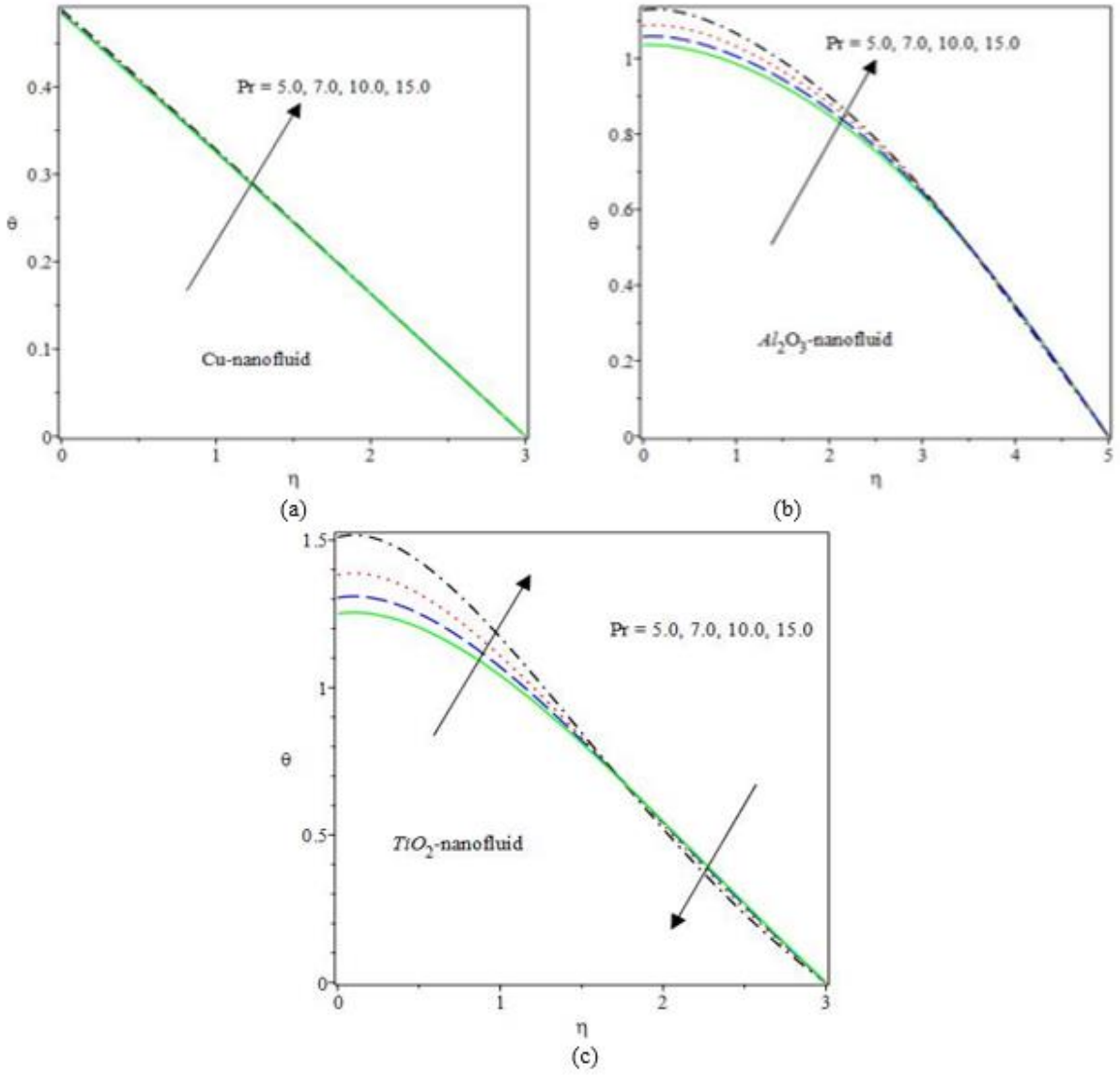

Fig. 8. Profile of $\theta(\eta)$ for different values of Pr (a) for Cu (b) for Al_2O_3 (c) for TiO_2

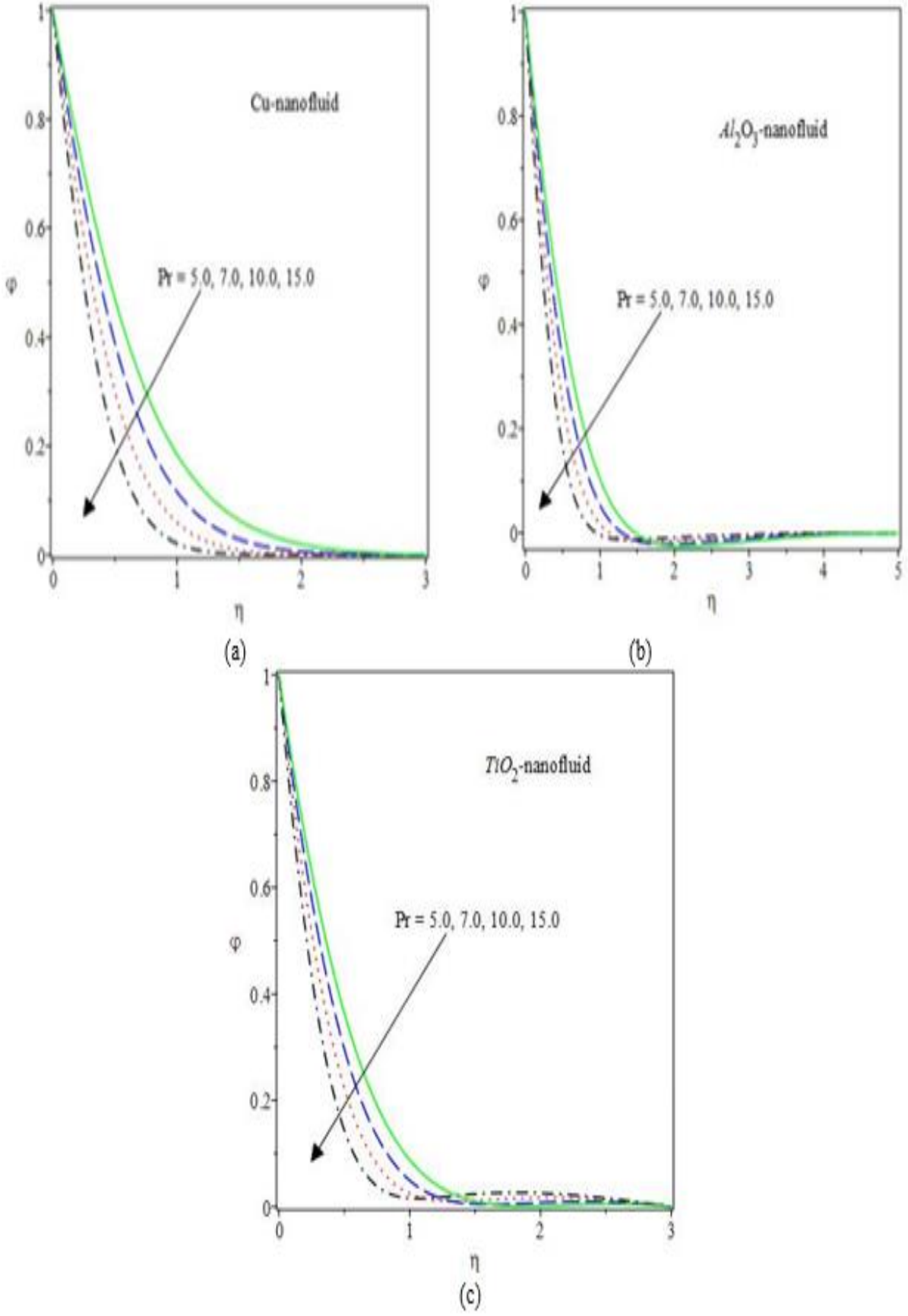

Fig. 9. Profile of $\varphi(\eta)$ for different values of Pr (a) for Cu (b) for Al_2O_3 (c) for TiO_2

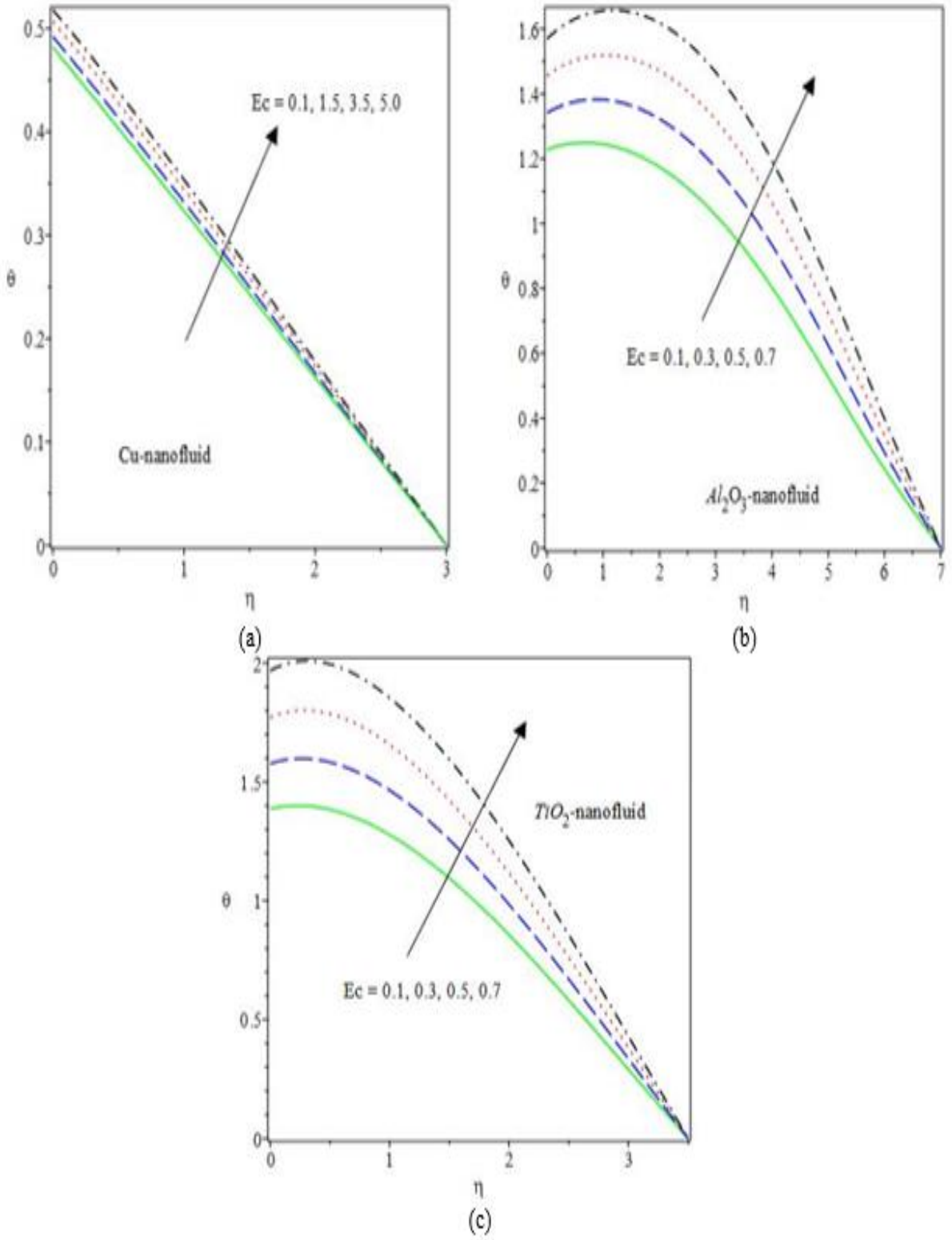

Fig. 10. Profile of $\theta(\eta)$ for different values of Ec (a) for Cu (b) for Al_2O_3 (c) for TiO_2

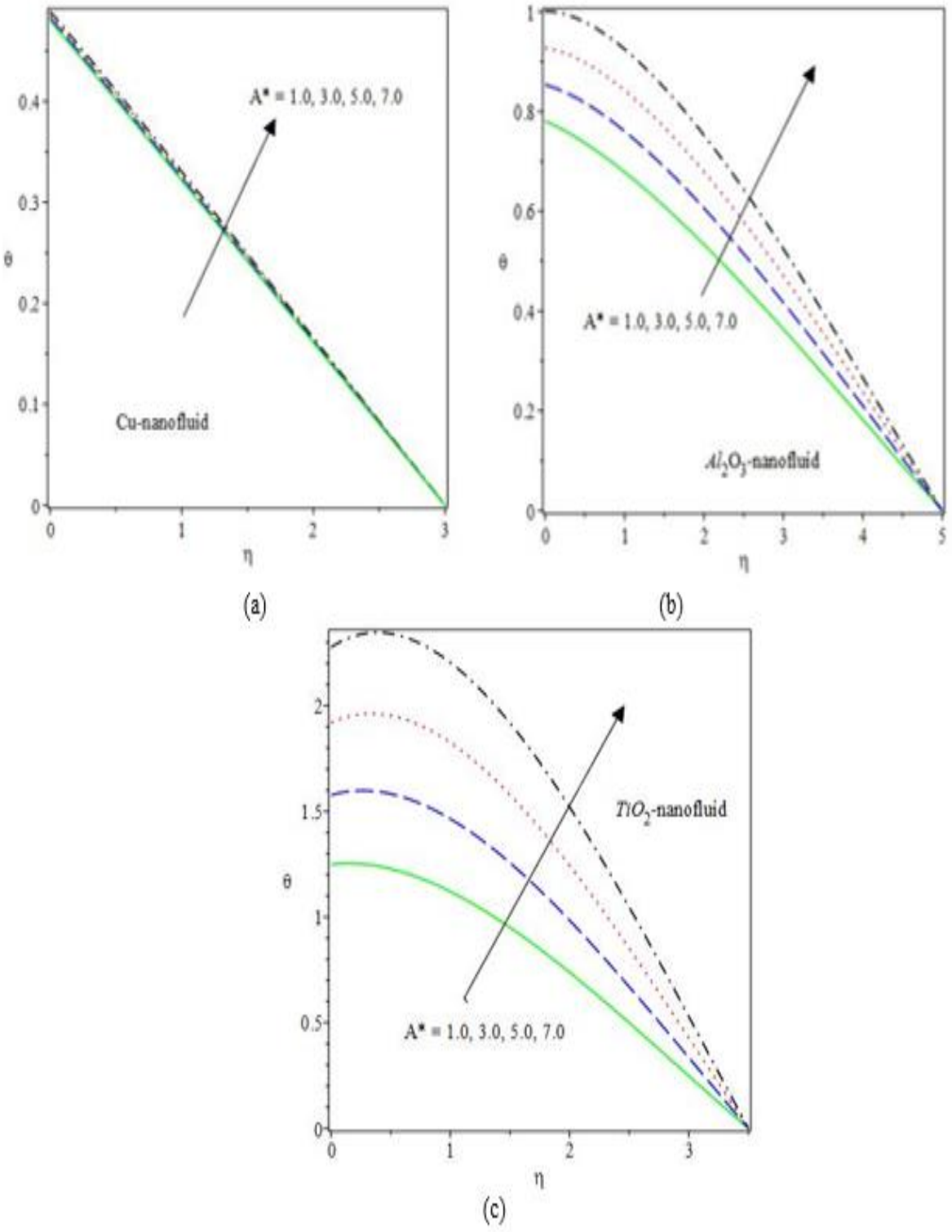

Fig. 11. Profile of $\theta(\eta)$ for different values of A^* (a) for Cu (b) for Al_2O_3 (c) for TiO_2

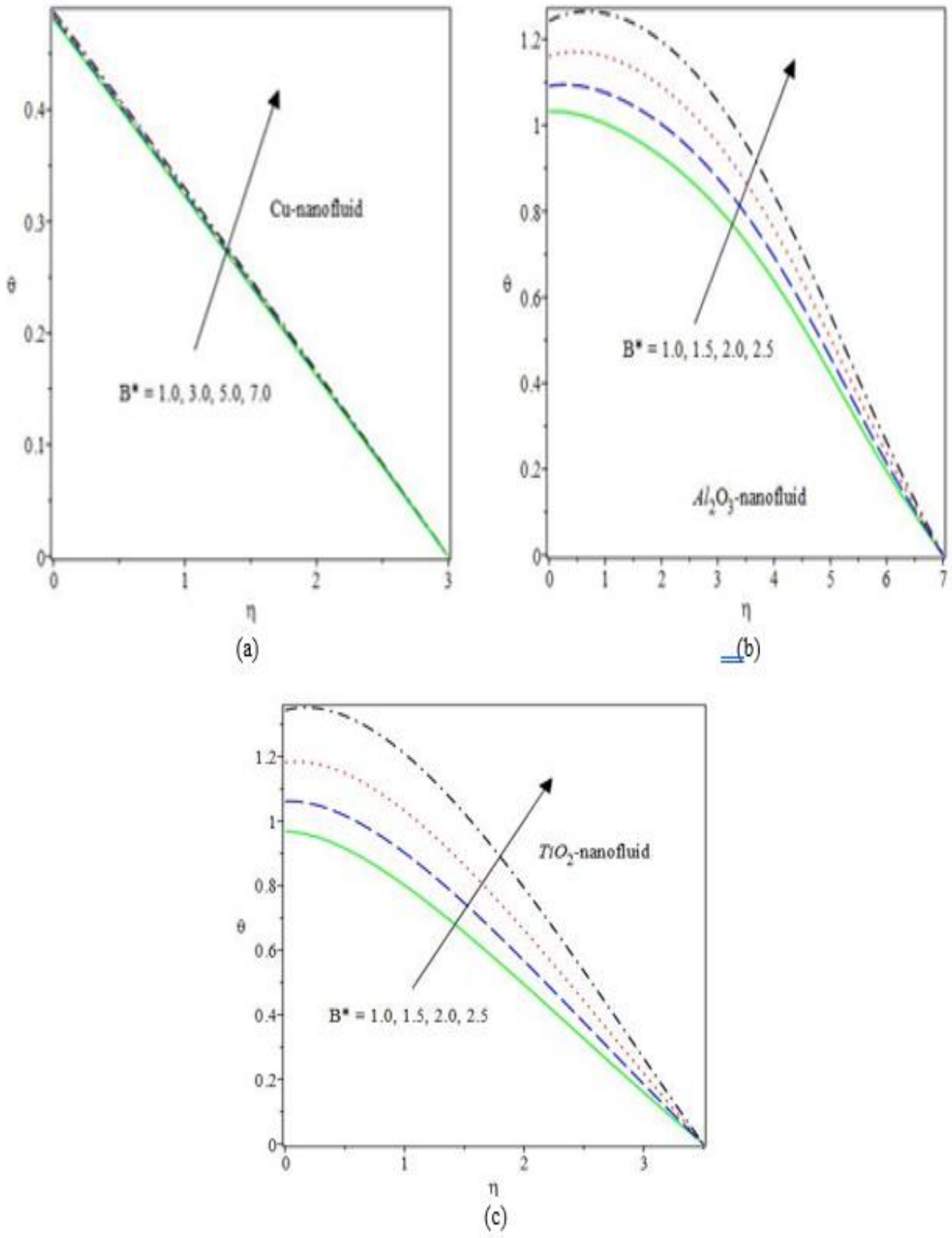

Fig. 12. Profile of $\theta(\eta)$ for different values of B^* (a) for Cu (b) for Al_2O_3 (c) for TiO_2

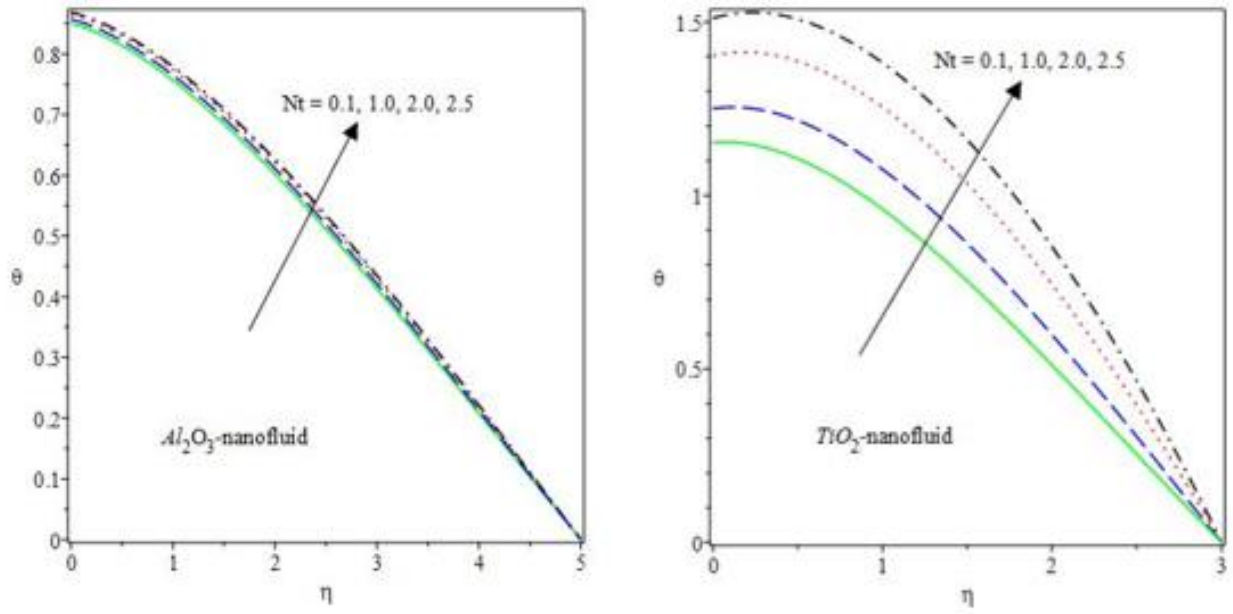

(a) (b)

Fig. 13. Profile of $\theta(\eta)$ for different values of Nt (a) for Al_2O_3 (b) for TiO_2

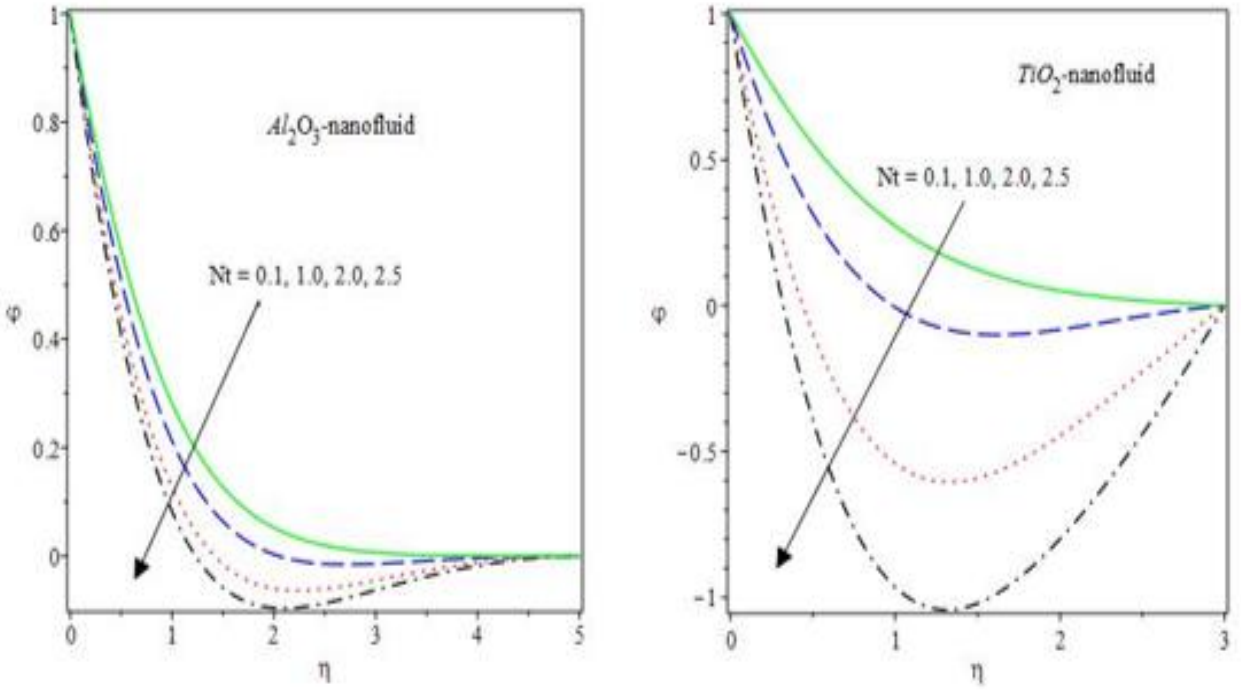

(a) (b)

Fig. 14. Profile of $\varphi(\eta)$ for different values of Nt (a) for Al_2O_3 (b) for TiO_2

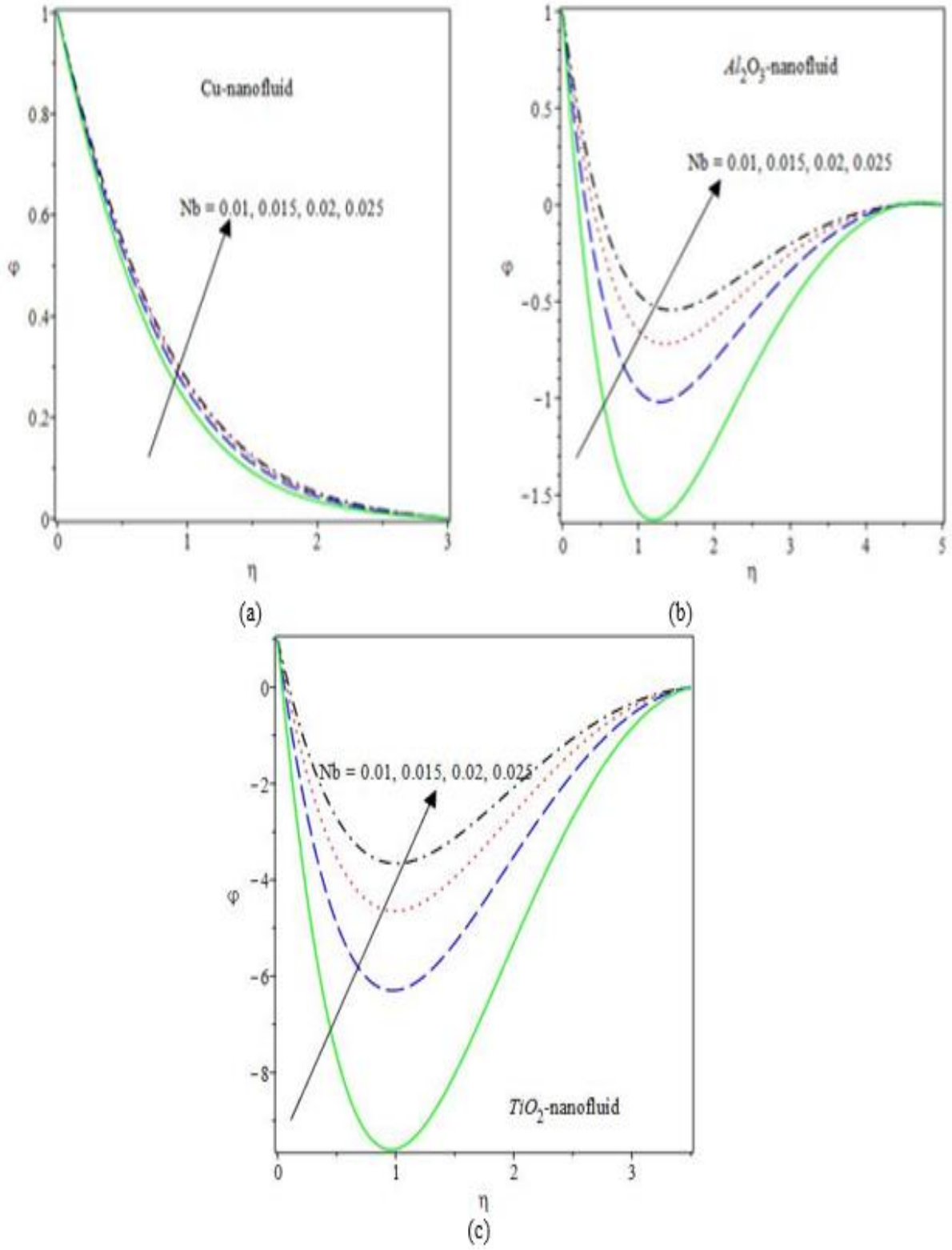

Fig. 15. Profile of $\varphi(\eta)$ for different values of Nb (a) for Cu (b) for Al_2O_3 (c) for TiO_2

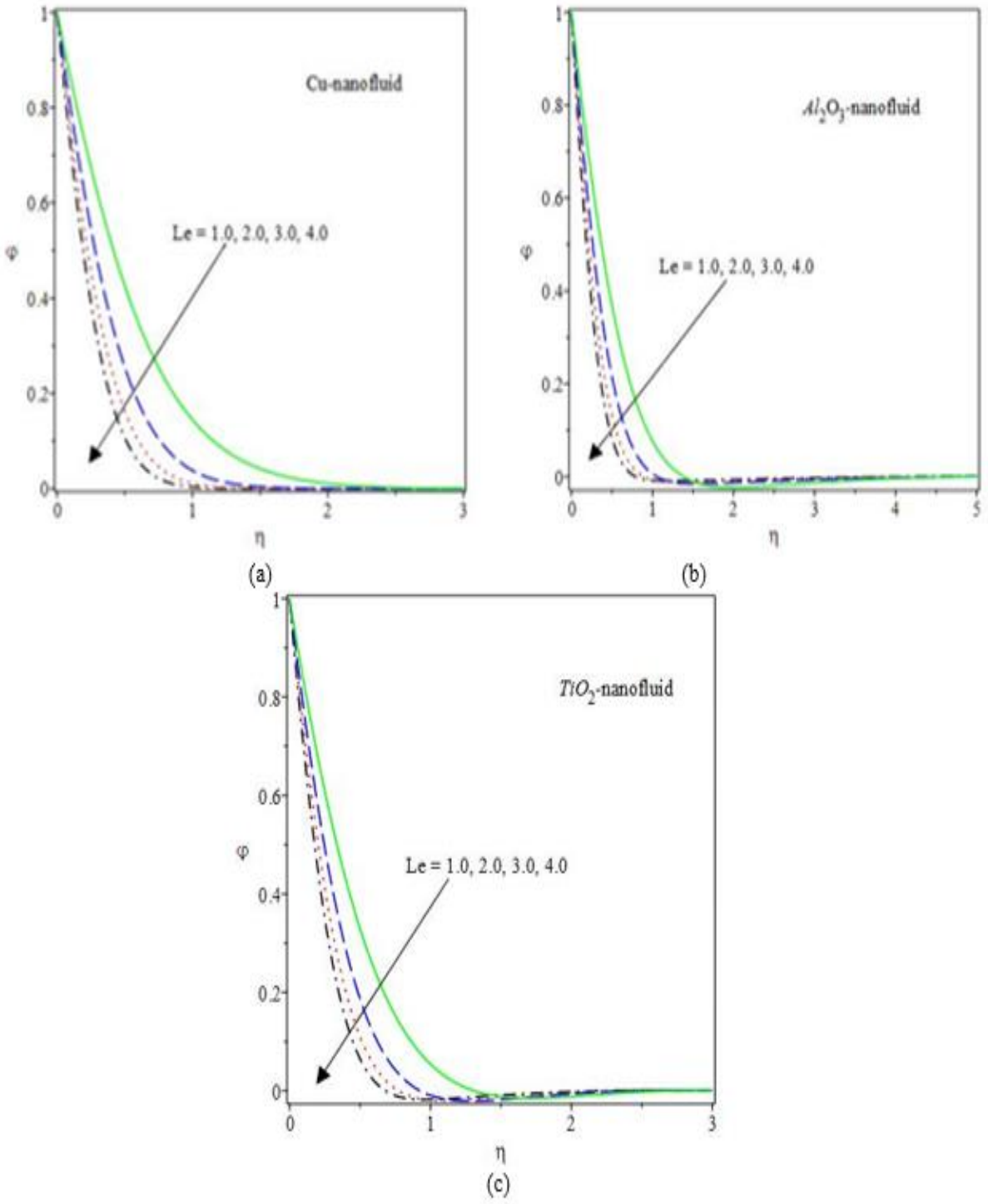

Fig. 16. Profile of $\varphi(\eta)$ for different values of Le (a) for Cu (b) for Al_2O_3 (c) for TiO_2

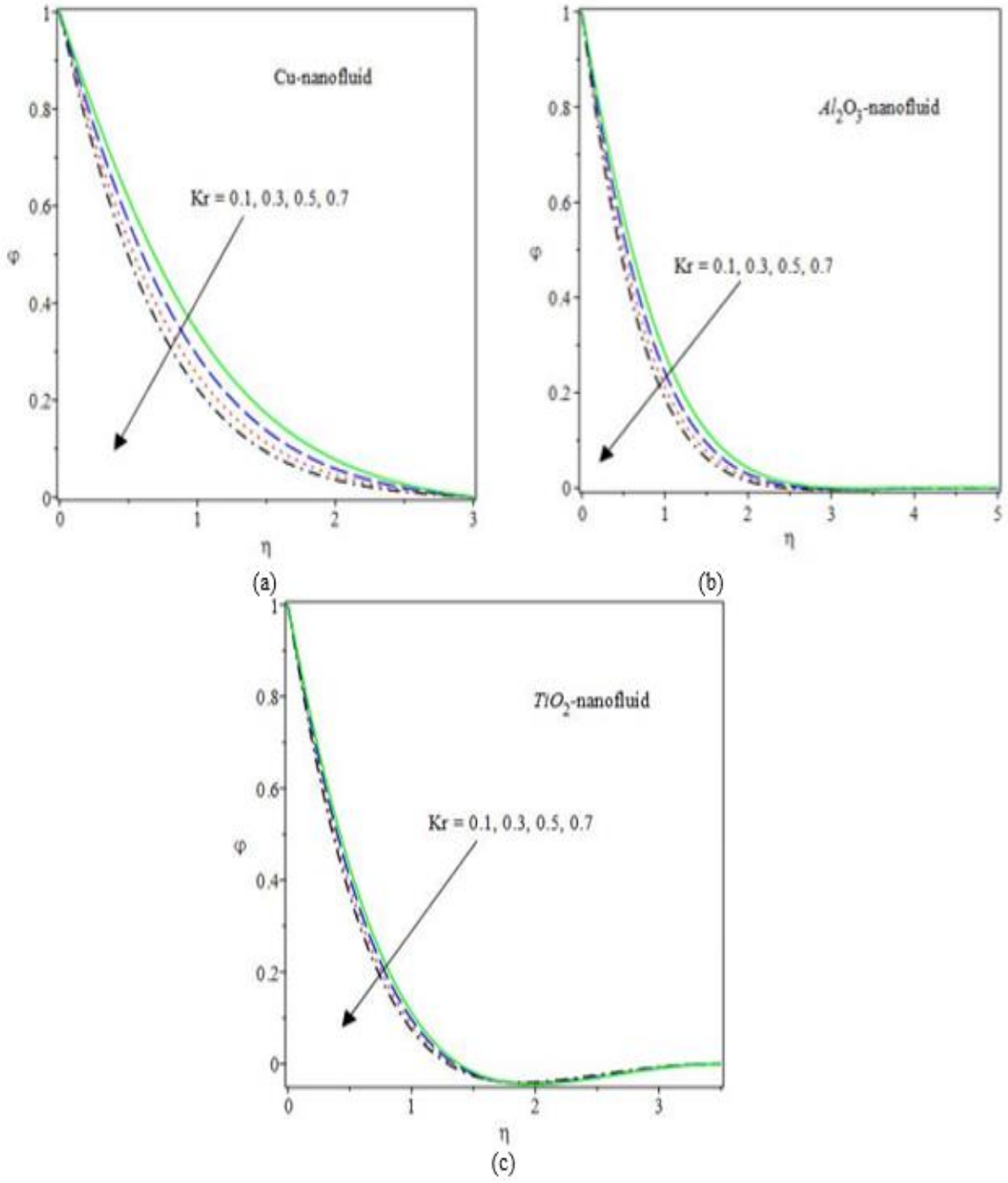

Fig 17. Profile of $\varphi(\eta)$ for different values of Kr (a) for Cu (b) for Al_2O_3 (c) for TiO_2

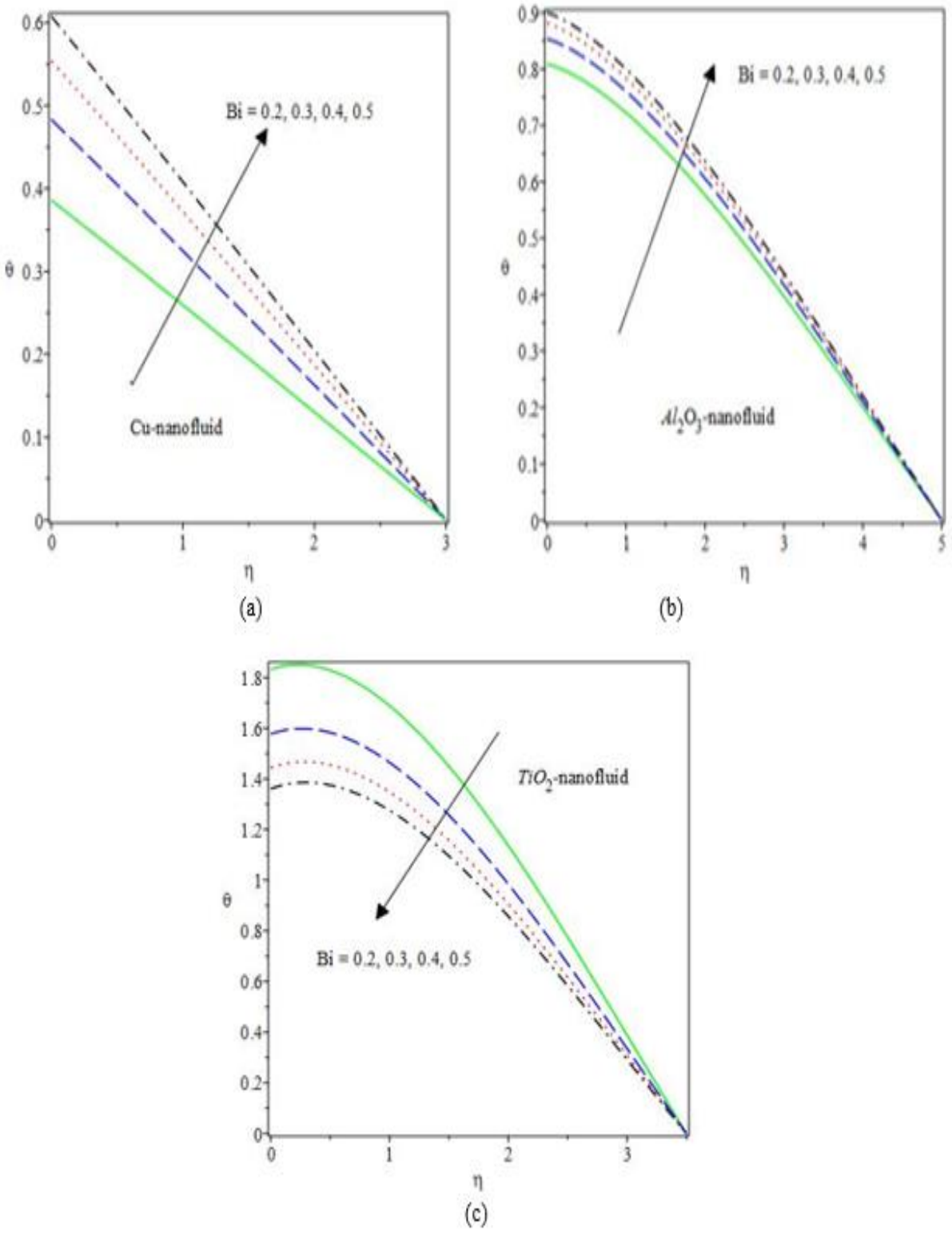

Fig. 18. Profile of $\varphi(\eta)$ for different values of Bi (a) for Cu (b) for Al_2O_3 (c) for TiO_2

Table 3: Computed values for various physical quantities of Al_2O_3 -nanofluid

M	Nt	Pr	R	C_f	Nu_x	Sh_x
1.0	0.5	0.3	0.5	-1.1597725754	0.0439446098	1.0773743636
1.5				-1.3918919728	0.0462649128	1.0439915233
2.5				-1.7392846786	0.0446961475	1.0082289767
	0.1			-1.1597603673	0.0448332937	1.0048211902
	1.0			-1.1597899082	0.0428256484	1.1702493672
		5.0		-1.0501733037	-0.0108071721	1.4556823916
		7.0		-1.0501503692	-0.0173619518	1.7143448193
			1.0	-1.1597864524	0.0446940200	1.0764925158
			3.0	-1.1598392926	0.0475490441	1.0731311577

Table 4: Numerical results for different physical quantities of Cu-nanofluid

Kr	Le	Nt	M	C_f	Nu_x	Sh_x
0.1				-1.3305420317	0.1550528736	0.8455525898
0.5				-1.3306425026	0.1550529768	1.1507249311
	1.0			-1.3307594112	0.1550530980	1.4212928606
	2.0			-1.3309105978	0.1550532005	2.0774096233
		0.010		-1.3306698259	0.1550530084	1.2221022617
		0.015		-1.3306412289	0.15505297823	1.1365593038
			3.5	-2.1734691678	0.15481300663	0.88808253795
			5.0	-2.5372839458	0.15463275886	0.86397872835
0.25	0.5	0.5	1.0	-1.1597725754	0.0439446098	1.0773743636

Table 5: Computed results for diverse physical quantities of TiO_2-nanofluid

A^*	B^*	Ec	Bi	C_f	Nu_x	Sh_x
3.0	3.0	0.3	0.3	-1.1597725754	0.0439446098	1.0773743636
1.0				-1.1957957045	-0.0746292359	1.3221899459
5.0				-1.1945897207	-0.2756298182	1.6366279295
	1.0			-1.1963287504	0.0095078885	1.1950850944
	2.0			-1.1959384234	-0.0543582532	1.2934654983
		0.1		-1.1955336919	-0.1162146306	1.3846346051
		0.5		-1.1948713956	-0.2310633775	1.5694484888
			0.2	-1.1947985881	-0.1663703286	1.5285136266
			0.5	-1.1955508937	-0.1801900603	1.4328266872

Figs. 2(a)-(c) illustrate the velocity distributions for different mixed convection parameter, $\lambda = Gr_x / \mathrm{Re}_x^2$ with $\lambda > 0$ (assisting flow) the flow is weakly accelerated for Cu nanoparticles whereas the converse behavior is induced for $\lambda < 0$ (opposing flow). The opposite response is generated in Al_2O_3 and TiO_2 i. e. opposing flow (negative mixed convection parameter) produces acceleration whereas assisting flow (positive mixed convection parameter) induces deceleration.

Figs. 3(a)-(c) depict the response in velocity distributions to modified Weissenberg viscoelastic parameter $\alpha^* = \alpha\,\Gamma$. This parameter modifies many shear terms in the momentum Eqn. (10) i.e. $-M_2(+\alpha^* f^2 f''' - 2\alpha^* f f' f''), -M_3 M(f' - \alpha^* f f'')$. The viscous drag experienced is enhanced with Weissenberg number. This leads to a consistent deceleration in the nanopolymer boundary layer flow for all three nanoparticles and the different metallic nanofluids are equally affected. Momentum diffusion is therefore inhibited by increasing

viscoelasticity of the nanofluid and there is a corresponding increase in momentum (hydrodynamic) boundary layer thickness.

Figs. 4(a)-(c) display the evolution in velocity distributions with increment in magnetic body force parameter, M, $M = \sigma_f B_0^2 / a\rho_f$ and features in the linear Lorentzian magnetohydrodynamic term, $-M_3 M(f' - \alpha^* f\ f'')$ in Eqn. (10). This body force inhibits the flow and acts transverse to the applied magnetic field i.e. along the sheet extrusion direction. Increasing M values amplify the magnetic drag which decelerates the boundary layer flow and opposes momentum diffusion as observed all three nanoparticle cases. When $M = 0$ the Lorentz force vanishes and the electrically non-conducting polymer case is retrieved and maximum velocity magnitudes and a thin momentum boundary layer is produced. However, as M exceeds unity, the momentum boundary layer is progressively thickened due to flow retardation. In magnetic nanomaterials processing therefore significant flow control may be produced with strategic selection of magnetic field strength which enables engineers to modify the internal constitution of nano-polymers. Asymptotically, smooth profiles are computed in the free stream indicating that a sufficiently large infinity boundary condition has been prescribed in the numerical simulations.

Figs. 5(a)-(c) display the temperature profiles for different values of magnetic body force parameter, M. The supplementary work expended by the nano-polymer in dragging against the action of the transverse magnetic field is dissipated as thermal energy i. e. heat. This increases temperatures for all three metallic nanoparticles, although copper nanofluid temperatures are only weakly enhanced whereas there is a progressively stronger temperature boost in Al_2O_3 and TiO_2 water nanofluids. Thermal boundary layers are therefore much thicker for TiO_2 compared with Al_2O_3 nanofluids and a much thinner thermal boundary layer arises for copper water nanofluid.

Figs. 6(a)-(c) display the nanoparticle concentration plots for different values of magnetic body force parameter, *M*. With increasing *M* values i. e. stronger magnetic body force, there is a clear accentuation in copper and Al_2O_3 concentration magnitudes at all locations transverse to the sheet; however, a marked decrease is induced for the case of TiO_2 nanoparticles. Nanoparticle concentration (species) boundary layer thickness is therefore enhanced for copper and alumina nanoparticles whereas it is reduced for titania-water nanofluid. Again very smooth distributions are computed in the free stream verifying that a sufficiently large infinity boundary condition has been prescribed in the MAPLE Chebyshev collocation computations.

Figs. 7(a)-(c) visualize the evolution in temperatures with radiative parameter, $R = \left(16\sigma_1 / 3k_1 k_f\right) T_\infty^3$. The radiative flux term, $(M_5 + R)\theta''$ in the energy (thermal) boundary layer Eqn. (12) augments the thermal conduction effect. When $R > 1$ thermal conduction dominates and vice versa for $R < 1$. For $R = 1$ both modes contribute equally. Greater radiative flux (lower R values) energize the nanopolymer regime which boosts temperatures. This increases thermal boundary layer thickness. Furthermore, considerably higher temperatures are achieved with Al_2O_3 compared with TiO_2 nanoparticles. Although the Rosseland model is relatively simple compared with other radiative heat transfer approaches, it does capture the correct influence of radiation on the thermal characteristics.

Figs. 8(a)-(c) visualize the response in temperatures with Prandtl number, $\Pr$. Prandtl number is inversely proportional to effective thermal conductivity of the magnetic nanofluid. $\Pr = 5$ corresponds to dense gases and $\Pr = 7$ approximates aqueous (water-based) polymeric fluids. $\Pr = 15$ is associated with low density molecular

polymeric solutions. As Pr is increased, thermal conductivity of the nanofluid is decreased. The heat transported by molecular conduction is therefore suppressed whereas convective transport is enhanced. This boosts temperatures for copper and alumina cases (Figs. 8a, b) and increases thermal boundary layer thickness. Cooling of the stretching sheet regime is therefore achieved with lower Prandtl number whereas heating is observed with higher Prandtl numbers. There is anomalous behavior for the TiO_2 nanoparticle case however (Fig 8c) further from the wall (sheet) where a depression in temperatures is induced with increasing Prandtl number.

Figs. 9(a)-(c) illustrate the distributions in nanoparticle concentrations with Prandtl number, Pr .Thermal diffusion rate is decreased with increasing Prandtl number. Similarly, the species diffusion rate is also adversely affected, via coupling with the energy and concentration boundary layer equations. This results in a strong depletion in nanoparticle concentration magnitudes. A very sharp descent arises relatively close to the wall and all three metallic nanoparticles exhibit a similar response with thinner species boundary layers.

Figs. 10(a)-(c) illustrate the distributions in temperature with Eckert number, Ec . $Ec = U_0^2 / \left\{(c_p)_f (T_f - T_\infty)\right\}$ *and, expresses the relative contribution of kinetic energy in the nanopolymer flow to the boundary layer enthalpy difference.* It features in both viscous (mechanical) heating i. e. $+M_1 \,\mathrm{Pr}\, Ec\, f''^2$ and Ohmic (Joule) magnetic dissipation i. e. $+M_3 \,\mathrm{Pr}\, Ec\, M\, f'^2 + M_4$. Even relatively small values of Ec exert a significant influence on thermal field. While a notable enhancement is induced in copper-water nanofluid temperatures, however, there is a much stronger accentuation in the Al_2O_3 (c) for TiO_2 water nanofluid temperatures i. e. thermal boundary layer thickness is much greater than for copper. Clearly dissipation effects correspond to substantial heat generation in the regime and this manifests in temperature elevations at all values of transverse coordinate, η .

Figs. 11(a)-(c) present the temperature profiles for various thermal space parameters, A^* . This parameter features in Eqn. (6) in the uneven heat source/sink term and appears in the dimensionless energy eqn. (11) as $\left\{+A^* f'\right\}$. Clearly elevation in this term will boost temperature which explains the trends in the figures. However, a more profound elevation in temperatures is associated with Al_2O_3 and TiO_2 nanoparticles, relative to copper nanoparticles. A much thinner thermal boundary layer is therefore associated with copper than the other two nanoparticles.

Figs. 12(a)-(c) present the temperature profiles for various heat source/sink parameters, B^* . This parameter also features in Eqn. (6) in the uneven heat source/sink term and appears in the dimensionless energy eqn. (11) in the linear term, $+B^*\theta$. Physically heat generation ($B^* > 0$) i. e. a thermal source, may be associated with a thermal hot spot in the sheet which is used in materials processing. A thermal sink is also used for cooling control $(B^* < 0)$. A very weak increase in temperature is generated for copper (Cu) nanoparticles with greater heat source and the response is linear. Maximum temperature is computed at the sheet surface in accordance with the boundary conditions imposed and temperatures vanish in the free stream. A much stronger enhancement in temperature is produced in Al_2O_3 and TiO_2 cases and with increasing heat source parameter, B^* , the profile topologies become increasingly parabolic. A significant temperature overshoot is only computed for the highest value of B^* close to the wall. Thermal boundary layer thickness is therefore strongly accentuated for Al_2O_3 and TiO_2 cases, but weakly increased for Cu .

Figures 13 (a)-(b) display the temperature values, $\theta(\eta)$ for different values of Nt (a) for Al_2O_3 (b) for TiO_2. Since no tangible modification for copper nanoparticles has been computed the plot is omitted. The thermophoresis parameter, Nt, arises in both the energy conservation (11) and nano-particle species conservation (12) boundary layer equations, specifically in the second-degree temperature gradient term, $+M_4 \Pr\left\{Nt\,\theta'^2\right\}$ and the second order temperature term, $+(Nt/Nb)\theta''$ in which it is also coupled with the Brownian motion parameter, Nb. It is therefore expected to influence both thermal and nanoparticle species diffusion $Nt = \tau D_T (T_f - T_\infty)/T_\infty \nu_f$ and is clearly a function of temperature difference across the boundary layer. Larger values of thermophoresis parameter, Nt, correspond to elevated migration of hot nanoparticles in the direction of a *decreasing temperature gradient* which encourages nano-particle diffusion in the boundary layer. Thermophoretic forces exerted on the nanoparticles are in the *opposite direction* to the actual temperature gradient. This results in a weak elevation in temperatures in Al_2O_3 but a much more dramatic elevation for TiO_2. Inevitably this response is intimately associated with the thermal and viscosity characteristics of both metallic nanofluids. A strong thickening of the thermal boundary layer is therefore instigated in the magnetic nanopolymer coating for TiO_2 whereas a much weaker one is produced in the Al_2O_3 case. No temperature overshoot is witnessed in the TiO_2 case but a marked trend is computed for the Al_2O_3 case and the overshoot is amplified with increment in Nt.

Figures 14 visualize the evolution in nanoparticle concentration, $\varphi(\eta)$ for different values of Nt (a) for Al_2O_3 (b) for TiO_2. Again, we have neglected the copper case since significant changes were not computed in temperature over a wide spectrum of thermophoresis parameter values. A substantial decrease in nanoparticle concentration magnitudes is produced for Al_2O_3 and an even more prominent reduction in TiO_2. The nanoparticle species diffusion is evidently inhibited with greater Nt values which results in a thinner nano-particle concentration boundary layer thickness. Therefore, thermophoresis induces the opposite response in the nano-particle concentration to the temperature distribution.

Figure 15 depicts the response in nanoparticle concentration $\varphi(\eta)$ for different values of Nb (a) for Cu (b) for Al_2O_3 (c) for TiO_2. $Nb = \tau D_B (C_f - C_\infty)/\nu_f$ as defined earlier. It is influenced by the concentration difference in nanoparticles from the wall to the free stream among other effects. It features in the energy conservation eqn. (11) in the term, $+M_4 \Pr\left\{Nb\,\theta'\,\varphi\right\}$ and also in the nano-particle concentration eqn. (12) in the term, $+(Nt/Nb)\theta''$. In both cases it is coupled with the temperature function, θ. With increasing Nb, there is a weak increase in Cu nano-particle concentration with a maximum computed near the wall. However, with greater Nb values the nano-particle concentration is much more profoundly boosted for Al_2O_3 and TiO_2 cases, again at all values of transverse coordinate. In the Buongiorno model the parameter Nb is inversely proportional to the size of nanoparticles (which are assumed spherical and homogenously distributed in the base fluid). With greater Nb values smaller nanoparticles are present and this intensifies the thermal conduction heat transfer from the particles to the surrounding fluid. This achieves the thermal enhancement which characterizes nanofluids and simultaneously for this regime, it boosts the molecular diffusion of nanoparticles and encourages migration through the base fluid

and intensifies ballistic collisions. Physically increased concentrations of nanoparticles (higher volume fractions) may therefore be produced in nano-coating design. There is an increase in nano-particle concentration boundary layer thickness with larger values of the Brownian motion parameter. Asymptotically smooth distributions are computed in the free stream again testifying to the prescription of an adequately large infinity boundary condition in the MAPLE code.

Figure 16 present the $\varphi(\eta)$ profiles for different values of Le (a) for Cu (b) for Al_2O_3 (c) for TiO_2 nanoparticles, respectively. Lewis number, $Le = \alpha_f / D_B$. It arises only in the nanoparticle concentration boundary layer Eqn. (12), in the first-degree term, $+Le\,\mathrm{Pr}\,(f\varphi')$. Lewis number embodies the relative rate of heat diffusion to the nano-particle diffusion rate. It also expresses the relative thickness of the thermal and nano-particle concentration boundary layers. For $Le = 1$, both boundary layers are of the same thickness and the diffusion rates are equal. For $Le > 1$ (of relevance in coating systems), the thermal diffusion rate exceeds the nano-particle diffusion rate and thermal boundary layer thickness is greater than nano-particle boundary layer thickness. There is therefore a significant reduction in nano-particle concentrations with greater Lewis numbers. In this case, the copper and TiO_2 show a much greater disparity in profiles than the Al_2O_3 nanoparticle case. However, for all nanoparticles the effect of Lewis number modification is clearly substantial. This behavior is sustained throughout the boundary layer regime transverse to the surface of the stretching sheet (coating). Nano-particle concentration boundary layer thickness is therefore markedly depleted with greater Lewis number. Lewis number overall observed to be a critical parameter determining the nano-particle distribution in the regime and manipulation of this parameter will inevitably be highly impactful in determining nano-coating homogeneity and constitution during manufacturing processes.

Figure 17 depict the distributions of $\varphi(\eta)$ for different values of Kr (a) for Cu (b) for Al_2O_3 (c) for TiO_2 with transverse coordinate. Nanoparticle concentrations are suppressed with increasing chemical reaction parameter, *Kr*, and the effect is strongest for copper-water nanofluid and weakest for TiO_2 water nanofluid. Clearly as more nanoparticles chemically react in a destructive homogenous reaction the original species is depleted. This reduces the concentration magnitudes, and also decreases nanoparticle concentration boundary layer thicknesses. A more significant decrement is computed for Cu and Al_2O_3 compared with TiO_2 nano-particles.

Figure 18 visualizes the nanoparticle concentration profiles, $\varphi(\eta)$ for different values of Bi (a) for Cu (b) for Al_2O_3 (c) for TiO_2. Increasing Biot number boosts the temperatures for copper and Al_2O_3 but reduces it for TiO_2 nanoparticles, and a linear response is computed for copper with a nonlinear profile for the other two nanoparticles. For small *Bi* values, thermally thin scenarios are relevant i. e. generally there are uniform temperature fields inside the body (nanopolymer sheet). Biot numbers much larger than 1 indicate thermally thick situations in which non-uniformity of temperature fields occurs. Nanoparticle species (concentration) boundary layer thickness is enhanced for copper and Al_2O_3 whereas it is suppressed for TiO_2 nanoparticles.

Table 3 show that with enhancing $M, Nt, \mathrm{Pr}\ and\ R$ the trends are as follows: with increasing magnetic parameter, M, skin friction, C_{fx} is increased whereas the Nusselt number Nu_x and Sherwood number Sh_x are reduced. With increasing Nt, skin friction is not changed but Nusselt number is reduced and Sherwood number elevated. With greater Prandtl number, skin friction is not affected but Nusselt and Sherwood numbers are

respectively decreased and increased in magnitude. With greater radiative parameter there is a weak increase in skin friction and Nusselt number but a slight reduction in Sherwood number. Table 4 shows that with increasing Kr skin friction is slightly increased as is Nusselt number; however, Sherwood number is strongly elevated. A similar response is observed with increasing Le values. The effects of M *and* Nt are as in Table 3. Finally, Table 5 shows the effects of A^*, B^*, Ec and Bi on skin friction, C_{fx}, Nusselt number Nu_x and Sherwood number Sh_x. Increasing A^* slightly increases the skin friction and Nusselt number magnitudes whereas it more strongly boosts the Sherwood number. Higher B^* (heat generation) parameter decreases skin friction, increases Nusselt number and also reduces Sherwood number. Greater Ec values decrease skin friction but increase Nusselt number and Sherwood number magnitudes. Finally increment in Biot number leads to an increase in skin friction and Nusselt number but reduces the Sherwood number.

5.CONCLUSIONS

Chebyshev collocation numerical solutions have been derived for incompressible mixed convection flow from a stretching sheet under the impact of Joule heating (Ohmic dissipation) and radiative heat flux. A combination of the Tiwari-Das and Buongiorno nanoscale models has been deployed. Three different water-based nanofluids with reactive metallic/oxide nanoparticles (Copper, Alumina and Titanium oxide) have been examined, of relevance to smart functional magnetic nano-polymers. Uneven heat source/sink, viscous dissipation, thermophoresis, Brownian motion and first order (homogenous and destructive) chemical reaction effects have been incorporated in the model. The upper convected Maxwell model has been utilized to analyze rheological (viscoelastic) nanofluid behavior and Rosseland's diffusion flux model for radiative heat transfer. Graphical results for velocity, temperature and nanoparticle concentration distributions have been presented for the different metallic-aqueous nanofluid cases. Validation has conducted with earlier published results, and excellent correlation achieved. Skin friction, local Nusselt number and local Sherwood number distributions have also been computed. The present simulations have shown that:

- Nanoparticle concentrations are reduced with increasing chemical reaction parameter and the effect is strongest for copper-water nanofluid and weakest for TiO_2 water nanofluid.
- Increasing Biot number boosts the temperatures for copper and Al_2O_3 but reduces it for TiO_2 nanoparticles, and a linear response is computed for copper with a nonlinear profile for the other two nanoparticles.
- Stronger magnetic field and Joule (Ohmic) dissipation decelerates the flow i. e. increases momentum boundary layer thickness and enhances temperatures (notably for TiO_2 nanoparticles).
- Increasing Eckert number elevates temperatures, most prominently for the Al_2O_3 and TiO_2 nanoparticles.
- Increasing heat generation boosts temperatures strongly for Al_2O_3 and TiO_2 nanoparticles but weakly for copper nanoparticles.
- An elevation in thermophoresis parameter strongly boosts the temperatures but suppresses nanoparticle concentration magnitudes.
- Higher Brownian dynamic parameter (corresponding to smaller spherical metallic nanoparticles) significantly elevates nanoparticle concentrations.

- Higher Weissenberg number (i. e. stronger viscoelastic effect) manifests in retardation in the boundary layer flow and an increase in momentum boundary layer thickness.

The current study has also demonstrated that the Chebyshev collocation numerical method is a powerful computational approach for solving nonlinear rheological multi-physical nanofluid coating flow problems. However, in the current work only Lorentzian magnetic body force has been addressed. Magnetic induction effects [70] which arise at higher magnetic Reynolds numbers feature a distortion in the magnetic field in the material. This is an important aspect in electro-inductive heating in polymer nano-coatings and may be studied in the future and may also consider simultaneous action of electrical fields and magnetic fields [71]. Finally, surface tension effects [72] may also be investigated which also contribute to momentum transfer characteristics in thermo-capillary phenomena in smart magneto-hydrodynamics.

ACKNOWLEDGMENTS

The authors express their sincere gratitude to the editor and reviewers for their suggestions which have improved the paper.

REFERENCES

[1] Han, Y. Mechanics of magneto-active polymers, PhD Thesis, Mechanical Engineering, Iowa State University, USA, (2012).

[2] Böker, A., Elbs, H., Hänsel, H., Knoll, A., Ludwigs, S., Zettl, H., Urban, V., Abetz, V., Müller, A. H. E. and Krausch, G. Microscopic mechanisms of electric-field-induced alignment of block copolymer microdomains, Physical Review Letters 89, 135502 (2002). https://doi.org/10.1103/physRevLett.89.135502

[3] Ze, Q., Kuang, X., Wu, S., Wong, J., Montgomery, S. M., Zhang, R., Kovitz, J. M., Yang, F., Qi, H. J. and Zhao, R. Magnetic Shape memory polymers with integrated multifunctional shape manipulation, Advanced Materials 32(4), 1906657 (2019). https://doi.org/10.1002/adma.201906657

[4] Xia, Y., He, Y., Zhang, F., Liu, Y. and Leng, J. A review of shape memory polymers and composites: mechanisms, materials, and applications, Advanced Materials 33(6), 119-126 (2020).

[5] Tekay, E. Thermo-responsive shape memory behavior of poly (styrene-b-isoprene-b-styrene)/ethylene-1-octene copolymer thermoplastic elastomer blends. Polymers for Advanced Technology 32(1), 428-438 (2020).

[6] Montgomery, S. M., Wu, S., Kuang, X., Armstrong, C. D., Zemelka, C., Ze, Q., Zhang, R., Zhao, R. and Qi, H. J. Magneto-mechanical metamaterials with widely tunable mechanical properties and acoustic bandgaps, Advanced Functional Materials 31, 3-10 (2020).

[7] Wang, T., Farajollahi, M., Choi, Y. S., Lin, I. T., Marshall, J. E., Thompson, N. M., Kar-Narayan, S., Madden, J. D. W. and Smoukov, S. K. Electroactive polymers for sensing, Interface Focus 6(4),1–19 (2016).

[8] Lovinger, A. J. Ferroelectric polymers, Science 220(4602),1115–1121 (1983).

[9] Richter, A., Kucking, D., Howitz, S., Gehring, T. and Amdt, K. F. Electronically controllable microvalves based on smart hydrogels: magnitudes and potential applications, Journal of Microelectromechanical Systems 12(5), 748–53 (2003).

[10] Kim, K. J. and Tadokoro, S. Electroactive Polymers for Robotic Applications, Artificial Muscles and Sensors, London: Springer (2007).

[11] Bird, R. B. and Armstrong, R. C. Dynamics of Polymeric Liquids (vol. 1, Ed.2). John Wiley & Sons, New York (1987).

[12] Shaw, M. T. Introduction to Polymer Rheology. Wiley, Wiley, New York (2012).

[13] Hayat, T., Saeed, Y., Alsaedi, A. and Asad, S. Effects of convective heat and mass transfer in flow of Powell-Eyring fluid past an exponentially stretching sheet, PLoS One 10, e0133831 (2015). https://doi.org/10.1371/journal.pone.0133831

[14] Shamshuddin MD., Anwar Bég, O., Ram, M. S. and Kadir, A. Finite element computation of multi-physical micropolar transport phenomena from an inclined moving plate in porous media, Indian Journal of Physics 92, 215–230 (2018).

[15] Anwar Bég, O., Zueco, J. and Ghosh, S. K. Unsteady natural convection of a short-memory viscoelastic fluid in a non-Darcian regime: network simulation, Chemical Engineering Communications 198, 172-190 (2010).

[16] Cramer, K. C. and Pai, S. I. Magnetofluid Dynamics for Engineers and Applied Physicists, McGraw Hill, New York (1973).

[17] Gazequiz, M. C., Hernandez, T., Muktepavela, F., Platacis, E. and Shishko, A. Magnetic field effect on the corrosion processes at the Eurofer–Pb–17Li flow interface, Journal of Nuclear Materials 465, 633-639 (2015).

[18] Yang, Y. S. and Huang, W. Magnetic field effects on coating deposition rate and surface morphology coatings using magnetron sputtering, Smart Materials and Structures 19, 124003 (2010). https://dx.doi.org/10.1088/0964-1726/19/12/124003

[19] Rohatgi, V. K. High temperature materials for magnetohydrodynamic channels, Bulletin of Material Science 6(1), 71-82 (1984).

[20] Davidson, P. A. Magnetohydrodynamic in materials processing, Annual Review of Fluid Mechanics 31, 273-300 (1999).

[21] Khan, M., Malik, R., Munir, A. and Shahzad. A. MHD flow and heat transfer of Sisko fluid over a radially stretching sheet with convective boundary conditions, Journal of Brazilian Society of Mechanical Science and Engineering 38,1279–1289 (2016).

[22] Gaffar, S. A., Prasad, V. R., Vijaya, B. and Anwar Bég, O. Mixed convection flow of magnetic viscoelastic polymer from a non-isothermal wedge with Biot number effects, International Journal of Engineering Mathematics 2015, 287623 (2015). https://doi.org/10.1155/2015/287623

[23] Salahuddin, T., Malik, M. Y., Hussain, A., Bilal, S. and Awais, M. Effects of transverse magnetic field with variable thermal conductivity on tangent hyperbolic fluid with exponentially varying viscosity, AIP Advances 5, 127103 (2015). https//doi.org/10.1063/1.4937366.

[24] Narla, V. K., Tripathi, D., Anwar Bég, O. and Kadir, A. Modelling transient magnetohydrodynamic peristaltic pumping of electroconductive viscoelastic fluids through a deformable curved channel, *Journal of Engineering Mathematics* 111,127–143 (2018).

[25] Ahmad, K., Honouf, Z. and Ishak, Z. Mixed convection Jeffrey fluid flow over an exponentially stretching sheet with magnetohydrodynamic effect, AIP Adv*ances* 6, 035024 (2016). https://doi.org/10.1063/1.4945401

[26] Bhatti, M. M., Zeeshan, A., Ijaz, N., Anwar Bég, O. and Kadir, A. Mathematical modelling of nonlinear thermal radiation effects on EMHD peristaltic pumping of viscoelastic dusty fluid through a porous medium channel, Engineering Science and Technology 20(3), 1129-39 (2017).

[27] Gaffar, S. A., Prasad, V. R., Anwar Bég, O., Khan, M. H. H. and Venkatadri, K. Radiative and Magnetohydro-dynamics flow of third grade viscoelastic fluid past an isothermal inverted cone in the presence of heat generation/absorption, Journal of Brazilian Society of Mechanical Science and Engineering 40,127-146 (2018).

[28] Manzoor, N., Anwar Bég, O., Maqbool, K. and Shaheen, S. Mathematical modelling of ciliary propulsion of an electrically conducting Johnson-Segalman physiological fluid in a channel with slip, Computer Methods in Biomechanical and Biomedical Engineering 22(7), 685-695 (2019).

[29] Asghar, Z., Ali, N., Sajid, M. and Anwar Bég, O. Micro-organism swimming propulsion through a shear rate-dependent biorheological fluid in an active channel assisted by a magnetic field, Journal of Magnetism and Magnetic Materials 486, 165283 (2019). https://doi.org/10.1016/j.jmmm.2019.165283.

[30] Madhavi, K., Prasad, V. R., Rao, A. S., Anwar Bég, O. and Kadir, A. Numerical study of viscoelastic micropolar heat transfer from a vertical cone for thermal polymer coating, Nonlinear Engineering (2019). https://doi.org/10.1515/nleng-2018-0064

[31] Shamshuddin, MD., Anwar Bég, O., Siva Reddy, S. and Kadir, A. Rotating unsteady multi-physico-chemical magneto-micropolar transport in porous media: Galerkin finite element study, Computational Thermal Sciences 10(2), 167–197 (2018).

[32] Shamshuddin, MD., Mishra, S. R., Anwar Bég, O. and Kadir, A. Unsteady reactive magnetic radiative micropolar flow, heat and mass transfer from an inclined plate with Joule heating: a model for magnetic polymer processing, Proceedings of IMechE-Part: C–Journal of Mechanical Engineering Science 223(4),1246-1261 (2019).

[33] Renardy, M. A matched solution for corner flow of the upper convected Maxwell fluid, Journal of Non-Newtonian Fluid Mechanics 58(1), 83–89 (1995).

[34] Zheng, L., Liu, N. and Zhang, X. Maxwell fluids unsteady mixed flow and radiation heat transfer over a stretching permeable plate with boundary slip and non-uniform heat source/sink, ASME Journal of Heat Transfer 135, 031705 (2013). https://doi.org/10.1115/1.4007891

[35] Bhatti, M. M., Shahid, A., Anwar Bég, O. and Kadir, A. Numerical study of radiative Maxwell viscoelastic magnetized flow from a stretching permeable sheet with the Cattaneo–Christov heat flux model, Neural Computing & Applications 30, 3467-3478 (2017).

[36] Hayat, T., Abbas, Z. and Sajid, M. MHD stagnation point flow of an upper-convected Maxwell fluid over a stretching surface. Chaos Soliton and Fractional *39*(2), 840–849 (2009).

[37] Motsa, S. S., Hayat, T. and Aldossary, O. M. MHD flow of upper-convected Maxwell fluid over porous stretching sheet using successive Taylor series linearization method, Journal of Applied Mathematics and Mechanics 33(8), 975–990 (2012).

[38] Mukhopadhyay, S. Heat transfer characteristics for the Maxwell fluid flow past an unsteady stretching permeable surface embedded in a porous medium with thermal radiation, Journal of Applied Mechanics 54(3), 385–396 (2013).

[39] Choi, S. U. S. Enhancing thermal conductivity of fluids with nanoparticle, *In: Developments and applications of non-Newtonian flows.* Siginer DA and Wang HP (eds). New York: American Society of Mechanical Engineers 231, 99–105 (1995).

[40] Buongiorno, J. Convective transport in nanofluids, ASME Journal of Heat Transfer 128, 240–250 (2006).

[41] Gonçalves, H. M. R., Pereira, R. F., Lepleux, E., Pacheco, L., Valente, A. J., Duarte, A. J. and de Zea Bermudez, V. Non-Newtonian Nanofluids: Non-Newtonian thermosensitive nanofluid based on carbon dots functionalized with ionic liquids. Nano-Micro Small 16(28), 2070156 (2020). https://doi.org/10.1002/smll.201907661

[42] Hojjat, M., Etemad, S. G., Baghen, R. and Thibault, J. Rheological characteristics of non-Newtonian nanofluids: Experimental Investigations, International Communication in Heat and Mass Transfer 38(2),144-148 (2011).

[43] Wang, B., Wang, X., Lou, W. and Hao, J. Thermal conductivity and rheological properties of graphite/oil nanofluids, Colloids and Surfaces A: Physicochemical Engineering Aspects 414, 125-131 (2012).

[44] Kole, M. and Dey, T. K. Effect of aggregation on the viscosity of copper oxide–gear oil nanofluids, International Journal of Thermal Science 50, 1741-1747 (2011).

[45] Kumar, M., Reddy, G. J., Kumar, N. N. and Anwar Bég, O. Computational study of unsteady couple stress magnetic nanofluid flow from a stretching sheet with Ohmic dissipation, Proceedings of IMechE-Part N: Journal of Nanoengineering Nanomaterial and Nanosystems 233(2-4), 49-63 (2019).

[46] Elgazery, N. S. Flow of non-Newtonian magneto-fluid with gold and alumina nanoparticles through a non-Darcian porous medium, Journal of Egyptian Mathematical Society 27, 39-50 (2019).

[47] Mehmood, R., Tabassum, R., Kuharat, S., Anwar Bég, O. and Babaie, M. Thermal slip in oblique radiative nano-polymer gel transport with temperature-dependent viscosity: solar collector nanomaterial coating manufacturing simulation, Arabian Journal of Science and Engineering 44, 1525-1541 (2018).

[48] Rana, P., Bhargava, R., Anwar Bég, O. and Kadir, A. Finite element analysis of viscoelastic nanofluid flow with energy dissipation and internal heat source/sink effects, International Journal of Applied and Computational Mathematics 3(2), 1421–1447 (2017).

[49] Rao, A. S., Nagendra, N., Amanulla, CH., Reddy, M. S. N. and Anwar Bég, O. Computational analysis of non-Newtonian boundary layer flow of nanofluid past a vertical plate with partial slip, Modelling, Measurement and Control B 86(1), 271-295 (2017).

[50] Ali, N., Zaman, A., Sajid, M., Anwar Bég, O., Shamshuddin, MD. and Kadir, A. Computational study of unsteady non-Newtonian blood flow containing nano-particles in a tapered overlapping stenosed artery with heat and mass transfer, Nanoscience Technology: An International Journal 9(3), 247–282 (2018).

[51] Nagendra, N., Rao, A. S., Amanulla, CH., Reddy, M. S. N. and Anwar Bég, O. Hydromagnetic non-Newtonian nanofluid transport phenomena past an isothermal vertical cone with partial slip: aerospace nanomaterial enrobing simulation, Heat Transfer-Asian Research 47(1), 203-230 (2017).

[52] Khan, W. A., Khan, M. and Malik, R. Three-dimensional flow of an Oldroyd-B nanofluid towards stretching surface with heat generation/absorption, PLoS One 9(8), e105107 (2014). https://doi.org/10.1371/journal.pone.0105107

[53] Ramesh, G. K., Roopa, G. S., Gireesha, B. J., Shehzad, S. A. and Abbasi, F. M. An electro-magneto-hydrodynamic flow Maxwell nanoliquid past a Riga plate: a numerical study, Journal of Brazilian Society of Mechanical Science and Engineering 39, 4547-4554 (2017).

[54] Mustafa, M., Khan, J. A., Hayat, T. and Alsaedi, A. Simulations for Maxwell fluid flow past a convectively heated exponentially stretching sheet with nanoparticles, AIP Advances 5, 037133 (2015). https://doi.org/10.1063/1.4916364

[55] Hayat, T., Ali, S., Awais, M. and Alhuthali, M. S. Newtonian heating in a Stagnation point flow of Burgers' Fluid, Applied Mathematics and Mechanics-England Edition 36(1), 61-68 (2015).

[56] Shamshuddin, MD., Mishra, S. R., Anwar Bég, O. and Kadir, A. Viscous dissipation and Joule heating effects in non-Fourier MHD squeezing flow, heat and mass transfer between Riga plates with thermal radiation: variational parameter method solutions, Arabian Journal of Science and Engineering 44, 8053-8066 (2019).

[57] Hayat, T. Qasim, M. Influence of thermal radiation and Joule heating on MHD flow of a Maxwell fluid in the presence of thermophoresis, International Journal of Heat and Mass Transfer 53, 4780–4788 (2010).

[58] Prasad, V. R., Rao, A. S. and Anwar Bég, O. Computational analysis of viscous dissipation and Joule heating effects on non-Darcy MHD natural convection from a horizontal cylinder in porous media with internal heat generation, Theoretical Applied Mechanics 41(1), 37-70 (2014).

[59] Hayat, T., Ali, S., Awais, M. and Alsaedi, A. Joule heating effects on MHD flow of Burgers' fluid, Heat Transfer Research 47(12), 1083-1092 (2016).

[60] Hayat, T., Ali, S., Alsaedi, A. and Al-Sulami, H. Influence of thermal radiation and Joule heating in the flow of Eyring-Powell fluid with Soret and Dufour effects, Journal of Applied Mathematics and Technical Physics 57 (6), 1051-1060 (2016).

[61] Anwar Bég, O., Hameed, M. and Bég, T. A. Chebyshev spectral collocation simulation of nonlinear boundary value problems in electro hydrodynamics, International Journal of Computer Methods in Engineering Science and Mechanics 14, 104-115 (2013).

[62] Elsayed, A. F. and Anwar Bég, O. New computational approaches for biophysical heat transfer in tissue under ultrasonic waves: Variational iteration and Chebyshev spectral simulations, Journal of Mechanics in Medicine and Biology 14(3), 1450043.1-1450043.17 (2014).

[63] Afify, A. A. and Elgazery, N. S. Effect of a chemical reaction on magnetohydrodynamic boundary layer flow of a Maxwell fluid over a stretching sheet with nanoparticles, Particuology 29, 154-161(2016).

[64] Sulochana, C., Ashwinkumar, G. P. and Sandeep, N. Effect of thermophoresis and Brownian moment on 2D MHD nanofluid flow over an elongated sheet, Defect and Diffusion Forum 377, 111-126 (2017).

[65] Aghamajidi, M., Yazdi, M. E., Dinarvand, S. and Pop, I. Tiwari-Das nanofluid model for magnetohydrodynamics (MHD) natural convective flow of a nanofluid adjacent to a spinning down-pointing vertical cone, Propulsion and Power Research 7(1), 78-90 (2017).

[66] Anwar Beg, O., Kuharat, S., Ferdows, M., Das, M., Kadir, A. and Shamshuddin, MD. Modeling magnetic nanopolymer flow with induction and nanoparticle solid volume fraction effects: Solar magnetic nanopolymer fabrication simulation, Proceedings of IMechE-Part N: Journal of Nanoengineering Nanomaterial and Nanosystems 233(1), 27-45 (2019).

[67] Viskanta, R. and Bergman, T. L. Heat transfer in materials processing. Warren M. Rohsenow; James P. Hartnett; Young I. Cho (Editors): Handbook of Heat Transfer, McGraw-Hill, New York (1998).

[68] Gebhart, B., Jaluria, Y., Mahajan, R. L. and Sammakia, B. Buoyancy-induced Flows and Transport, Hemisphere, Washington (1988).

[69] Das, S. K., Choi, S. U. S., Yu, W. and Pradeep, T. Nanofluids: Science and Technology, Wiley, New York (2007).

[70] Uddin, M. J., Kabir, M. N., Anwar Bég, O. and Alginahi, Y. Chebyshev collocation computation of magneto-bioconvection nanofluid flow over a wedge with multiple slips and magnetic induction, Proceedings of IMechE-Part N: Journal of Nanoengineering Nanomaterial and Nanosystems 232(4), 109-122 (2018).

[71] Zohra, F. T., Uddin, M. J., Ismail, A. I. M. and Anwar Bég, O. Bioconvective electromagnetic nanofluid transport from a wedge geometry: simulation of smart electro-conductive bio-nano-polymer processing, Heat Transf.-Asian Research 47(1), 231-250 (2018).

[72] Shamshuddin, MD., Mishra, S. R., Anwar Bég, O., Bég, T. A. and Kadir, A. Computation of radiative Marangoni (thermocapillary) magnetohydrodynamic convection in Cu-water based nanofluid flow from a disk in porous media: smart coating simulation, Heat Transfer 50(3), 1931-1950 (2020).

APPENDIX

Notations

Nomenclature

a	Stretching rate [1/s]	Bi	Biot number
Al_2O_3	Alumina nanoparticle	A^*	Thermal space parameter
B^*	internal heat source (sink)	B_0	Magnetic field strength
C	species concentration [kg/m^2]	C_w	Sheet surface concentration
C_∞	ambient nanoparticle concentration	C_f	Dimensionless drag force
Cu	Copper nanoparticle	C_p	Specific heat [J/Kg K]
D_B	Brownian coefficient [m^2/s]	D_T	Thermophoresis coefficient [m^2/s]
Ec	Eckert number	h	Step size
h_f	Coefficient of heat transfer	J_w	Mass transport rate
k_1	Mean absorption coefficient	Kr	Chemical reaction parameter
k_{nf}	Maxwell-Garnetts thermal conductivity [Wm^{-1}K^{-1}]	Le	Lewis number
M	Magnetic parameter	N	Concentration buoyancy
Nb	Brownian motion parameter	Nt	Thermophoresis parameter
Nu_x	Local Nusselt number	Pr	Prandtl number
q_r	Radiative heat flux [W/m^2]	q_w	heat transport rate
R	Thermal radiation parameter	Re_x	Local Reynolds number
T	Fluid temperature [K]	TiO_2	Titanium oxide nanoparticle
T_f	Convective temperature [K]	T_w	Temperature at the wall [K]
T_∞	Ambient temperature [K]	u, v	Velocity components [m/s]
u_w	Plate velocity [m/s]	x	Distance along the surface [m]

y Distance normal to surface [m]

Greek symbols

τ	Heat capacity ratio (nanoparticle to base fluid)	τ_w	shear stress
β_T	Volumetric thermal expansion	β_C	volumetric solutal expansion
ρ_f	Base fluid density [kg/m^3]	ρ_{nf}	density of nanoparticles [kg/m^3]
$(\rho c_p)_{nf}$	Heat capacity	μ_{nf}	Brinkmann effective viscosity [kg m^{-1}s^{-1}]
σ_1	Stefan-Boltzmann constant	σ_{nf}	electrical conductivity [$\Omega^{-1}m^{-1}$]
ψ	Stream function [m^2/s]	η	similarity variable
λ	Mixed convection parameter	δ	optimal step size
Γ	Maxwell viscoelastic parameter	θ	dimensionless temperature
φ	Dimensionless concentration	ϕ	solid volume fraction

Subscripts

w	quantities at wall	∞	quantities far away from surface
f	Base fluid	nf	Nanofluid